TITLE

Partial input loss differentially modifies neural pathways

AUTHORS

Joo Yeun Lee[1✢], David B. Kastner[3], Scott C. Harris[1], Luca Della Santina[2], Jeremiah V. John[1], Natalia S. Stone[1], and Felice A. Dunn[1✢]

AFFILIATIONS:

[1]Department of Ophthalmology
University of California, San Francisco
San Francisco, CA 94143-0518, USA

[2]College of Optometry
University of Houston
Houston, TX 77204-2020, USA

[3]Department of Psychiatry and Behavioral Sciences
University of California, San Francisco
San Francisco, CA 94143-0518, USA

Corresponding authors contacts:
✢Felice.Dunn@ucsf.edu, JooYeun.Lee@ucsf.edu

✢ Lead Contact

SUMMARY (200 word limit)

Following input loss from degeneration, injury, and/or aging, downstream circuits undergo modifications that can impact fundamental sensory computations. Using the retina to leverage known cell types, well-defined circuitry, and molecular tools, we show how multiple pathways adjust their functional properties differently to common input loss and further locate these changes within each pathway. Specifically, we asked if two OFF ganglion cell types, alpha OFF-sustained (A_{OFF-S}) and OFF-transient (A_{OFF-T}) cells, and their respective dominant presynaptic partners, type 2 and type 3a cone bipolar cells, respond differentially to partial cone

loss. We find that $A_{OFF\text{-}T}$ ganglion cells exhibit more circuit changes than $A_{OFF\text{-}S}$ ganglion cells, resulting in altered spatiotemporal tuning following partial cone loss. We show that the underlying mechanisms include changes in glutamatergic, GABAergic, and glycinergic circuits in the pathway of $A_{OFF\text{-}T}$ ganglion cells. In response to common input loss, our study finds different locations of circuit modifications across OFF pathways. These distinct functional changes in two pathways contribute to maintaining perceptually relevant information, preserving key visual features despite input loss. These findings provide insight into how sensory systems can compensate to ultimately serve vision.

INTRODUCTION

Across sensory systems, neuronal pathways can undergo distinct changes in response to deafferentation[1–5]. The mechanisms underlying these differential responses and their implications for potential pathway-specific repair remain open questions. Given the dynamic properties of our nervous system even when natural regeneration is not possible, achieving optimal sensory restoration through artificial intervention requires systematic examination of the states of remaining circuitry in response to deafferentation and following rescue. Our understanding of that degeneration process is severely limited: while we know that neurons can die, we lack understanding of how the death of neurons in one part of a circuit influences information processing downstream. Using the retina's well-characterized circuits, we precisely controlled the degree of cone death to understand whether partial cone loss has pathway-specific effects downstream. Visual signals transmitted from photoreceptors diverge at the dendrites of bipolar cells, the second-order neurons of the mammalian retina, into 15 pathways[6]. These secondary pathways further diverge into >30 types of ganglion cells with diverse functional properties[7–14]. In studies of injury and disease, specifically animal models of optic nerve crush, glaucoma, and retinitis pigmentosa, certain ganglion cell types tend to be more vulnerable[15–18], suggesting that injury can differentially affect cell types. However, how different ganglion cell types differentially respond to common input loss remains unknown. Answering such a question has important implications for understanding how downstream neurons respond to common sensory input loss, which occurs in normal aging, neurodegeneration, and injury. Therefore, we asked how these different pathways change upon photoreceptor loss. Previously, we demonstrated how the alpha ON-sustained ($A_{ON\text{-}S}$) ganglion cells, the mouse orthologue of primate ON midget ganglion cells[19], react to partial loss of cones in the mature retina[20,21]. The loss of cones caused changes to the spatial receptive field of $A_{ON\text{-}S}$ ganglion cells, including narrower centers and wider surrounds[20,21]. Paradoxically, this

result resembles spatial receptive field changes that occur in response to increases in light levels, rather than what is expected to occur under low light levels or low signal to noise ratio with fewer inputs[22,23]. Consistent with this interpretation, cone loss could masquerade as more light because fewer cones would release less glutamate, potentially placing the retina in a light adapted state. If so, the signatures of light adaptation may be present across pathways. In this study, we ask if two OFF pathways exhibit global light-adapted characteristics or undergo unique pathway-specific changes after cone loss.

To answer this question, we selectively ablated cones in the adult mouse retina[20,21] and examined the anatomical and functional properties across retinal pathways. We focus on two types of OFF ganglion cells: the alpha OFF-sustained ($A_{OFF\text{-}S}$) and alpha OFF-transient ($A_{OFF\text{-}T}$) ganglion cells, the mouse orthologs of primate OFF midget and OFF parasol ganglion cells, respectively[19]. $A_{OFF\text{-}S}$ ganglion cells receive dominant inputs from type 2 (T2) and $A_{OFF\text{-}T}$ ganglion cells are primarily driven by type 3a (T3a) OFF cone bipolar cells[24,25]. T2 and T3a OFF cone bipolar cells exhibit distinct temporal tuning properties[26] and ramify at different inner plexiform layer (IPL) depths to target $A_{OFF\text{-}S}$ and $A_{OFF\text{-}T}$ ganglion cells, respectively[25]. Differential dynamics in these ganglion cells are thought to originate from glutamate receptors at the bipolar cell dendrites[27,28], transmission from bipolar cells to ganglion cells, and inputs from amacrine cells[7,29,30].

Because different ganglion cell types showed differential responses upon insult or disease[15,16], we examined whether these two OFF pathways exhibit common and/or differential responses to the loss of a shared input, aiming to understand how each pathway is impacted by damage. Specifically, can the responses to cone loss be localized to changes before or after the divergence of these two OFF pathways? If partial cone loss induces common changes to both $A_{OFF\text{-}S}$ and $A_{OFF\text{-}T}$ ganglion cells, it would indicate circuitry changes before divergence of, i.e., shared inputs to, the OFF pathways (Figure 1A). Changes could occur at one or more of the following locations: cones, horizontal cells, and/or common amacrine cells. If $A_{OFF\text{-}S}$ and $A_{OFF\text{-}T}$ ganglion cells exhibit differential reactions to partial cone loss, it would indicate circuitry changes after divergence of, i.e., different inputs to, the OFF pathways. Changes could occur at one or more of the following locations: bipolar cells (T2 to $A_{OFF\text{-}S}$ and T3a to $A_{OFF\text{-}T}$), presynaptic amacrine cells (unique ACs to T2 or T3a), and direct amacrine cells (unique ACs to $A_{OFF\text{-}S}$ or $A_{OFF\text{-}T}$) (Figure 1A)[31]. We find evidence for modifications across retinal circuits, e.g., changes in excitatory and inhibitory inputs to two A_{OFF} ganglion cells, suggesting that the retina is not

ubiquitously in a light-adapted state following partial cone loss. Such results are significant in demonstrating differential reactions to common input loss, their underlying mechanisms, and the potential for rescue across multiple pathways for sensory processing.

RESULTS

Partial cone loss causes differential temporal changes to A_{OFF} ganglion cell types

To examine how the structure and function of retinal pathways were affected by partial cone loss, we ablated a subset of cones in mature retina by injecting diphtheria toxin (DT) into mice expressing the simian DT receptor under the M-opsin promoter at postnatal day 30 (cone-DTR) [20,21]. The concentration of DT was adjusted to achieve a 50-70% reduction of cones (Figure S1A-B). We examined how cone loss impacts the functional responses of OFF pathways. We targeted either A_{OFF-S} or A_{OFF-T} ganglion cells for single-cell recordings (Figure 1A). Cone-mediated inputs were elicited under three conditions: full stimulation of control retina (control), full stimulation of partial cone loss retina (cone-DTR), and partial stimulation of control retina (partial) (Figure 1B). To determine whether changes to the spatiotemporal filter induced by partial cone loss are distinct from partial stimulation, we modified a stimulus by blanking half the space to simulate unresponsive cones[20,21]. To determine the site of changes, we used different recording configurations to isolate inputs to and outputs from A_{OFF} ganglion cells: voltage clamp to record excitatory and inhibitory input currents and current clamp to record output spikes and subthreshold voltages (Figure 1F-G, S2, S3). Each recording configuration of a ganglion cell type was used to generate a linear spatiotemporal filter (Figure 1F).

First, we focus on the temporal component of the ganglion cell spatiotemporal filters (Figure 1G). There are many different aspects to the temporal filter, and we do not know, a priori, which, if any, might change. Therefore, we performed principal components analysis of the temporal filters under all conditions (Figure 1H, S2B, S3B) to extract the features that vary the most, and compared the strength of the projection onto the first principal component across conditions (Figure 1I-J, S2, S3). To understand the mechanisms underlying changes to the temporal filter, we made pairwise comparisons of the three conditions (control vs. cone-DTR, control vs. partial stimulation, cone-DTR vs. partial stimulation) (Figure 1B-E). For voltage temporal filters, A_{OFF-T} ganglion cells showed differences between cone-DTR vs. partial stimulation and control vs. partial stimulation, but not between control vs. cone-DTR (Figure 1I). This result implicates compensation, i.e., a mechanism that allows responses in cone-DTR

retina to match those in the full stimulation of control retina, but not match those from partial stimulation (Figure 1E). For excitatory temporal filters, $A_{OFF\text{-}T}$ ganglion cells showed significant differences in control vs. cone-DTR and cone-DTR vs. partial, but not between control vs. partial stimulation (Figure 1J). This result implicates circuit changes, i.e., a mechanism underlying changes observed in cone-DTR that causes responses to be better or worse than control (Figure 1D). While we emphasize the comparisons in which significant differences were detectable, several comparisons result in undetectable differences despite cone loss or partial stimulation, which could indicate recovery (Figure 1B). In another possible result, differences in control vs. cone-DTR and control vs. partial stimulation, but not between cone-DTR vs. partial stimulation, would implicate half cone stimulation as the mechanism for changes observed in cone-DTR (Figure 1C). Other combinations of comparisons are interpreted as inconclusive (Figure S2A), for example, excitatory temporal filters of $A_{OFF\text{-}S}$ ganglion cells (Figure S3G). Such inconclusive results could be consistent with either ½ cone or compensation; however, further studies would be required to distinguish those possibilities. For all other recording conditions (i.e., inhibition and spikes), no evidence of a difference was observed across conditions (Figures S2, S3).

The identification of a difference in one cell type and not the other is insufficient to conclude that there is a differential effect between the cell types[32]. Therefore, to quantify the relative differences between the two ganglion cell types, we compared the sum of differences between each condition and the other two, e.g., (control - cone-DTR) + (control - partial), between the two cell types. This metric describes how distinct one condition is from other conditions (Figure 1K). $A_{OFF\text{-}T}$ ganglion cells undergo greater changes in the excitatory temporal filter compared to $A_{OFF\text{-}S}$ ganglion cells (Figure 1L); however, there was no evidence for a difference between cell types in the inhibitory temporal filters (Figure S2E). Similarly, temporal filters for spikes and subthreshold voltages were not significantly different between the two cell types (Figure S3E and I). Therefore, we find evidence that the temporal filters from excitatory currents exhibited distinct circuitry changes after the point of divergence between $A_{OFF\text{-}S}$ and $A_{OFF\text{-}T}$, i.e., at T3a cone bipolar cell inputs to $A_{OFF\text{-}T}$ ganglion cells.

We next identified which features of the temporal filter changed in the excitatory currents to explain the difference seen in the $A_{OFF\text{-}T}$ ganglion cells (Figure 1M). Qualitatively, following partial cone loss, the temporal filter lost its biphasic component (Figure 1N). To test this quantitatively, we measured the extent to which modifying each of five features, i.e., time to peak, time to

trough, peak amplitude, trough amplitude, time to zero, made the control temporal filter more or less like the mean cone-DTR temporal filter. Briefly, this was achieved by linearly modifying each feature of individual control filters, and then measuring the projection of these modified filters along the vector that points from the mean control filter to the mean cone-DTR filter, where a value of 0 is equivalent to the mean control filter and a value of 1 is equivalent to the mean cone-DTR filter (see Methods, Figure S2F-H). Time to peak, time to trough, peak amplitude, and trough amplitude each contribute approximately 0.2 units normalized distance to the difference between control and cone-DTR temporal filters. Time to zero crossing contributed the most by shifting the temporal filter 0.8 units of normalized distance from the control and cone-DTR temporal filters (Figure 1O). Taken together, we conclude that following partial cone loss the changes in excitatory temporal filters of $A_{OFF\text{-}T}$, but not $A_{OFF\text{-}S}$, ganglion cells reflect circuit mechanisms, mostly captured by a delay in the time to zero crossing.

Two distinct mechanisms in inhibitory circuits underlie changes in temporal filters of $A_{OFF\text{-}T}$ ganglion cells

To reveal the circuit mechanisms underlying the temporal changes following partial cone loss, we measured excitatory and inhibitory temporal filters of $A_{OFF\text{-}S}$ and $A_{OFF\text{-}T}$ ganglion cells in control and cone-DTR retina in the absence and presence of picrotoxin, an antagonist of $GABA_A$ and $GABA_C$ receptors, or strychnine, an antagonist of glycine receptors. We analyzed temporal filters to determine the contributions of GABAergic or glycinergic inhibition.

We evaluated the effect of the GABAergic (Figure 2A, D, F, O) or glycinergic (Figure 2B, E, J, S) antagonists within and between each control and cone-DTR condition. To this end, we first subtracted the temporal filters before and after pharmacological blockade for each cell to compute a difference filter (Figure 2C). Then with the difference filters, we performed principal component analysis on the control and cone-DTR conditions of $A_{OFF\text{-}S}$ and $A_{OFF\text{-}T}$ ganglion cells (Figure 2G, K, P, T). First, we found significant differences between control and cone-DTR under glycinergic inhibition of excitatory temporal filters of $A_{OFF\text{-}T}$ ganglion cells (Figure 2L). Therefore, we attributed the mechanism underlying the changes in cone-DTR to presynaptic glycinergic inhibition (Figure 2N). Second, in inhibitory temporal filters of $A_{OFF\text{-}T}$ ganglion cells, we observed significant differences between control vs. cone-DTR conditions under GABAergic, but not glycinergic blockade (Figure 2Q and U). We attributed the mechanism underlying changes in cone-DTR to direct GABAergic inhibition (Figure 2O-R, W). In the next layer of comparison

between $A_{OFF\text{-}S}$ and $A_{OFF\text{-}T}$ ganglion cells, we found no significant differences between the cell types (Figure 2I, M, R, V).

Taken together, these data provide evidence for two modifications to circuits of the $A_{OFF\text{-}T}$ ganglion cell's temporal filters following partial cone loss, i.e., changes in (1) presynaptic glycinergic inhibition, consistent with changes in excitatory temporal filters (Figure 1L) and (2) direct GABAergic inhibition which could mask differences in inhibitory temporal filters (Figure S2E). While definitive mechanisms could not be assigned to inhibitory temporal filters for the $A_{OFF\text{-}S}$ ganglion cells, we also did not find significant differences between the two ganglion cell types.

Partial cone loss causes differential spatial changes in A_{OFF} ganglion cell types

Having observed changes to the temporal dimension of the ganglion cell responses, we next determined how partial cone loss affected spatial processing of these OFF pathways. We compared spatial filters obtained from $A_{OFF\text{-}S}$ vs. $A_{OFF\text{-}T}$ ganglion cells under three conditions of control, cone-DTR, and partial stimulation, and under different recording configurations to separate inputs and outputs (Figure 3A). We applied the same framework as described for the kinetics to determine the contributions of half cone stimulation, circuit changes, and compensation to the spatial filters of each cell type (Figure 1B-E); to compare spatial differences between two cell types (Figure 1K); and to determine if these mechanisms arise prior to or after divergence between the OFF pathways.

Principal component analysis was performed on the entire spatial filter for excitation, inhibition, spikes, and subthreshold voltages (Figure 3A-B). The projection onto the first principal component of the spatial filters were significantly different across conditions. Based on these differences, we attribute the changes in the spatial filters to compensation in the $A_{OFF\text{-}T}$ inhibition (Figure 3D) and $A_{OFF\text{-}S}$ spikes (Figure 3F), and to circuit changes in the $A_{OFF\text{-}S}$ voltages (Figure 3I). In contrast, we found no evidence for any difference in the excitatory spatial filters between the two cell types (Figure S4). Though the data is consistent with different mechanisms for spatial inhibition and spikes, we did not find evidence for differential effects between $A_{OFF\text{-}S}$ and $A_{OFF\text{-}T}$ ganglion cells (Figure 3E, H); however, the two cell types were found to be significantly different for spatial voltages in the cone-DTR condition, implicating distinct circuit changes in

post-receptoral circuits, i.e., T3a cone bipolar cells and/or unique amacrine cell inputs (Figure 3K).

Similar to the way we analyzed the temporal filters, we next determined which features of the spatial filter changed in the voltages of A_{OFF-S} ganglion cells (Figure 3K) by assessing how modifying each feature of the control spatial filter better matches the cone-DTR filter (Figure S2F-H). Qualitatively, following partial cone loss, the surround of the spatial filter widened (Figure 3L-M). Quantitatively, while center and surround height and center width each contribute approximately 0.2 units to the difference between control (normalized value of 0) and cone-DTR (normalized value of 1) spatial filters, surround width contributes a shift of 0.85 units toward cone-DTR spatial filters (Figure 3N). Taken together, we conclude that following partial cone loss, the changes in voltage spatial filters of A_{OFF-S}, but not A_{OFF-T}, ganglion cells reflect circuit mechanisms mostly captured by a widening of the surround, which could arise from changes in amacrine cell inputs to A_{OFF-S} ganglion cells.

Two distinct mechanisms underlie changes in spatial filters of A_{OFF-T} ganglion cells

Next, we determined the mechanisms underlying the spatial changes following partial cone loss. We measured excitatory and inhibitory spatial filters of A_{OFF-S} and A_{OFF-T} ganglion cells in control and cone-DTR retina in the absence and presence of an antagonist of $GABA_A$ and $GABA_C$ receptors (Figure 4A, D, F, O), or an antagonist of glycine receptors (Figure 4B, E, J, S). With the difference filters of the spatial filters before and after pharmacological blockade for each cell (Figure 4C), we performed principal component analysis on the control and cone-DTR conditions of A_{OFF-S} and A_{OFF-T} ganglion cells (Figure 4G, K, P, T). First, we found no differences in the first principal components of the spatial filters between control vs. cone-DTR conditions under both GABAergic and glycinergic blockade; therefore, we attributed the mechanism underlying the changes in cone-DTR in the excitatory spatial filters of A_{OFF-S} and A_{OFF-T} ganglion cells to excitatory circuits (Figure 4F-N). Second, in both inhibitory temporal and spatial filters of A_{OFF-T} ganglion cells, we observed significant differences between control vs. cone-DTR conditions under GABAergic, but not glycinergic blockade (Figure 4Q and U). Therefore, we attributed the mechanism underlying changes in cone-DTR to direct GABAergic inhibition (Figure 4O-R, W). In the comparison between A_{OFF-S} and A_{OFF-T} ganglion cells, we found no significant differences between the cell types (Figure 4I, M, R, V).

The effects of pharmacology on spatial filters provide evidence for two modifications to circuits of the A_{OFF-T} ganglion cells following partial cone loss, i.e., changes in (1) excitation and (2) direct GABAergic inhibition. Modifications in the inhibitory spatial filters of A_{OFF-S} ganglion cells remain ambiguous without a clear mechanistic interpretation, and we also did not find significant differences between the two ganglion cell types.

Partial cone loss causes responses of A_{OFF-S} and A_{OFF-T} ganglion cells to decrease

The linear spatiotemporal filters described above map onto the cell's actual response with a nonlinearity, which reflects average changes in response magnitude to a given change in stimulus contrast. We used the same framework as described in quantifying temporal and spatial filters to compare nonlinearity differences between two cell types and to determine if these mechanisms arise prior to or after divergence between the OFF pathways. If the loss in cone inputs changes the cell's response differently from both full and partial stimulation of control conditions, this would suggest additional circuit changes following cone loss (Figure 1D). Indeed, the circuit change outcome was exhibited by underlying excitatory and inhibitory input currents which decreased more than predicted by partial cone stimulation (Figure 5A, C-D, F-G). Such decrease leads to differences when we compare PC1 across conditions and to the same extent in both cell types in cone-DTR retina (Figure 5C-D and F-G). This suggests additional functional deficits in the excitatory and inhibitory circuits to both ganglion cells.

Interestingly, while cone-DTR exhibits different nonlinearities from fully and partially stimulated control retina (Figure 5C-H), we found no evidence for differences in retinal outputs, as shown by spike nonlinearities of both cell types (Figure 5I-K). We evaluated whether cone loss had a differential effect on the nonlinearities of inputs and outputs across conditions. Cone loss resulted in greater changes in the nonlinearities of excitatory currents than that of spike outputs of A_{OFF-S} ganglion cells (Figure 6E) while this effect was not found in voltages of A_{OFF-S} ganglion cells (Figure 6F) nor of A_{OFF-T} ganglion cells (Figure 6M-N). Interestingly, the nonlinearities of inhibitory currents in cone-DTR retina showed greater changes compared to that of spikes and subthreshold voltage outputs in both cell types (Figure 6G-H, O-P), suggesting differential impact of cone loss on the nonlinearities of the two A_{OFF} cell types. Despite a lack of evidence for changes to the spike nonlinearities after cone loss, the subthreshold voltage nonlinearities of A_{OFF-T} ganglion cells from cone-DTR retina were different from full and partial stimulation of control retina (Figure 5M). One potential explanation is the increase of intrinsic excitability of

A_{OFF-T} ganglion cells following partial cone loss, which would lead to the recovered spike nonlinearity in A_{OFF-T} ganglion cells even with lower voltage responses. We tested this by measuring spikes in response to injected white noise currents into A_{OFF} ganglion cells under perforated patch-clamp configuration[12,20,21]. We found no evidence to support this possibility for both A_{OFF-S} and A_{OFF-T} ganglion cells (Figure S6A-F). However, changes in intrinsic properties, such as resting membrane potential and spike threshold, could be missed as the membrane potentials were artificially held at -60mV. Therefore, to capture intrinsic differences between these two cell types, we injected a slow ramp of current to induce spikes and examined the resting membrane potential and the threshold of current ramp-evoked spikes. We found that cone loss depolarized the resting membrane potential of A_{OFF-T} ganglion cells with a maintained spike threshold which accounts for steeper voltage-to-spike transformation (Figure S6G-H). Together, the equivalent changes in nonlinearity of input currents in both A_{OFF-S} and A_{OFF-T} ganglion cells suggest common effects of cone loss on two OFF pathways, and nonlinearity differences between spikes and subthreshold voltages arise from intrinsic differences between these two cell types, suggesting that in addition to cone loss affecting cone bipolar and amacrine cells, cone loss evoked differential changes at the level of ganglion cells.

Three distinct mechanisms underlie changes in nonlinearities of both A_{OFF-S} and A_{OFF-T} ganglion cells upon partial cone loss

Having found circuit changes to excitatory and inhibitory nonlinearities following partial cone loss (Figures 5-6), we evaluated the differences between the input current nonlinearities before and after GABAergic or glycinergic antagonists (Figure 7A-E) to determine the underlying mechanisms. The first principal components of the excitatory nonlinearity differences were not significantly different between control vs. cone-DTR conditions for both GABAergic and glycinergic blockade, suggesting changes in excitatory circuits to A_{OFF-S} and A_{OFF-T} ganglion cells of cone-DTR retina (Figure 7F-N). On the other hand, we found the first principal components of inhibitory nonlinearity differences from both ganglion cell types were significantly different between control vs. cone-DTR conditions under GABAergic blockade (Figure 7Q), suggesting changes in direct GABAergic inhibition onto A_{OFF-S} and A_{OFF-T} ganglion cells (Figure 7W). In addition, the first principal components of the inhibitory nonlinearity differences in A_{OFF-T} ganglion cells from cone-DTR were different from that of control retina under glycinergic blockade (Figure 7U). Therefore, we attributed the mechanism underlying changes to the nonlinearity of cone-DTR to both direct GABAergic and glycinergic inhibition (Figure 7W). Having found

functional evidence for glutamatergic, GABAergic, and glycinergic modifications following partial cone loss, we also examined synaptic puncta in the bipolar and ganglion cells of these two retinal pathways. We found a subset of the anatomical parameters correlated with functional findings (Figure S5).

Taken together, these data provide evidence for common modifications of excitatory circuits following partial cone loss in $A_{OFF\text{-}S}$ and $A_{OFF\text{-}T}$ ganglion cells. Additionally, inhibitory circuits undergo two distinct modifications: (1) direct GABAergic inhibition onto $A_{OFF\text{-}S}$ ganglion cells, and (2) direct GABAergic and glycinergic inhibition onto $A_{OFF\text{-}T}$ ganglion cells.

Following partial cone loss, spatiotemporal modifications have minimal consequences on the perception of natural movies

These ganglion cell spatiotemporal filters ultimately serve vision; therefore, we determined how the observed ganglion cell spatiotemporal modifications could contribute to preserve perceptually relevant information by using the measured spatiotemporal filters of subthreshold voltages applied to natural scenes. To quantify movies filtered by the receptive fields of (1) full stimulation of control retina, (2) cone-DTR retina, and (3) partial stimulation of control retina, we used two metrics to quantify the similarity between filtered and original movies: (a) the inverse of a mean squared error (MSE), which we call a non-perceptual similarity index, and (b) a perceptually relevant structural similarity index (SSIM) modeled off the human visual system, which evaluates three features of an image: luminance, contrast, and structure[21,33,34]. We previously showed that static natural images filtered by $A_{ON\text{-}S}$ ganglion cell spatial receptive fields following partial cone loss were indistinguishable from those filtered by control $A_{ON\text{-}S}$ ganglion cell spatial receptive fields when evaluated by the SSIM, the perceptual similarity index, but were significantly worse when evaluated by the non-perceptual similarity metric[21]. To address whether spatial and temporal filters from individual pathways show differences in the filtered movies, we included $A_{ON\text{-}S}$ ganglion cells in our comparison with both types of A_{OFF} ganglion cells (Figure 8). Now applied to natural movies, the non-perceptual image similarity, as quantified by 1/MSE, showed differences across conditions and cell types. When we compared across conditions within each cell type, we found that movies filtered by cone-DTR receptive fields of $A_{ON\text{-}S}$ and $A_{OFF\text{-}T}$ ganglion cells were significantly different from movies filtered by the control filters, while those filtered by $A_{OFF\text{-}S}$ ganglion cells were not significantly different in non-perceptual similarity (Figure 8C-E). However, such differences in $A_{OFF\text{-}T}$ ganglion cells were

not found when evaluated by SSIM (Figure 8H). In contrast, A_{ON-S} ganglion cells of cone-DTR retina showed lower SSIM compared to that of control (Figure 8F). When we compare between OFF cells, movies filtered by A_{OFF-T} ganglion cells in cone-DTR retina, which showed lower similarity in the rudimentary comparison of mean squared error, were perceptually indistinguishable from movies filtered by A_{OFF-T} ganglion cells in control retina (Figure 8G-H). In addition, we found differences across cell types. As expected, movies filtered by receptive fields of A_{ON-S} ganglion cells in all three conditions had greater similarity due to preserved polarity in both metrics (Figure S7A-F). Between the two OFF ganglion cell types, similarity quantified by 1/MSE was comparable in cone-DTR (Figure S7B), however, A_{OFF-T} ganglion cells showed higher perceptual similarity to the original movies compared to A_{OFF-S} ganglion cells (Figure S7E). Together, our results demonstrate heterogeneity between ON and OFF pathways in filtering natural movies as well as differences between two A_{OFF} ganglion cells, i.e., changes in spatiotemporal properties of A_{OFF-T} ganglion cells shapes their output to more effectively preserve perceptually relevant features of natural movies compared to A_{OFF-S} ganglion cells. These results suggest that spatial and temporal changes observed in A_{OFF-T} ganglion cells following partial cone loss contribute to preserving perceptually relevant features of natural movies.

DISCUSSION

Results demonstrate that both A_{OFF-S} and A_{OFF-T} ganglion cells undergo different temporal and spatial modifications in response to partial cone loss that cannot be recapitulated by partial stimulation of control mature retina, providing evidence for retinal circuit changes unique to each pathway. We compared differences in temporal and spatial properties across cone stimulation and cone loss conditions and categorized mechanisms for changes in cone-DTR retina. We found that A_{OFF-S} ganglion cells undergo compensatory changes and A_{OFF-T} ganglion cells undergo circuit changes which lead to differences in their linear temporal filters (Figure 1). Pharmacological manipulations revealed two mechanistic changes to the circuits of A_{OFF-T} ganglion cells for temporal filters following partial cone loss: presynaptic glycinergic inhibition and direct GABAergic inhibition (Figure 2). While voltage spatial filters revealed greater changes to A_{OFF-S} ganglion cells compared to A_{OFF-T} ganglion cells (Figure 3), pharmacological manipulations revealed changes in direct excitation and direct GABAergic inhibition to A_{OFF-T} ganglion cells could contribute to the difference between the two cell types (Figure 4). Lastly, we found circuit changes to both cell types affecting the nonlinearity (Figure 5). Both ganglion cells

exhibited a decreased response captured by the nonlinearity; however, differences in intrinsic properties accounted for recovered outputs (Figure 5-6). For the cell's actual response measured by its nonlinearity, pharmacological manipulations revealed two mechanistic changes to both A_{OFF-S} and A_{OFF-T} ganglion cells: direct excitation and direct GABAergic inhibition; and an additional mechanistic change to A_{OFF-T} ganglion cells, direct glycinergic inhibition (Figure 7). Each of these results support the conclusions that neither partial light stimulation alone nor light adaptation are sufficient to elicit the changes following partial cone loss. Finally, the accumulation of evidence that A_{OFF-T} ganglion cells exhibit more circuitry changes following partial cone loss resulted in a greater preservation of perceptually relevant features in natural movies filtered by cone-DTR receptive fields (Figure 8). Our study finds multiple sites of modifications in the retinal circuit after divergence of the two OFF pathways, indicating functional differences in response to common input loss. Such distinct circuit changes, in turn, contribute to preserving perceptually relevant information.

Previously, we showed that partial cone loss triggers changes in inhibitory circuits in the ON pathway, specifically in pathways leading to the A_{ON-S} ganglion cells. A_{ON-S} ganglion cells exhibited expansion of receptive field surrounds, greater temporal integration, recovery of inhibitory gain and enhancement of inhibitory synapses in the dendrites. We determined that inhibition compensates for fewer cones to preserve perception of static natural images[21]. Both ON and OFF pathways exhibited some common spatial changes following partial cone loss, i.e., surround expansion. Yet, we found a difference in adjusting kinetics across retinal pathways after cone loss[21] (Figure 1) consistent with previous studies in control retina[12,13]. Specifically, cone-DTR retina of A_{OFF-T} ganglion cells exhibited greater degree of changes in excitatory temporal filters compared to that of A_{OFF-S} ganglion cells. We speculate that while spatial changes were sufficient to maintain the quality of static images across cell types[21] (Figure S7I-L), temporal changes in A_{OFF-T} ganglion cells contribute to achieve higher perceptual similarity in filtering movies (Figure 8). Expansion of the surround and loss of the biphasic component could be attributed to potential changes in inhibition, for example, changes in inhibitory inputs onto A_{OFF-T} ganglion cells (Figure 2, 4, 7 and S5). At the same time, we found that changes in excitatory circuits are a common consequence of global disruption of cones. Future experiments assessing the potential upregulation of developmentally-expressed receptor subunits following cone loss will determine the contributions of GABAergic and glycinergic amacrine cells in shaping visual outputs[35]. A_{OFF-T} ganglion cells tend to be more vulnerable among the mouse ganglion cell types in other manipulations of the retinal circuit, e.g., models of

glaucoma and optic nerve crush[15,16]. Perhaps differences in manipulation cause differential responses across ganglion cell types and/or perhaps the plasticity of inhibitory circuits leading to the A_{OFF-T} ganglion cells render them robust in some conditions or up to certain thresholds of damage and then render them particularly vulnerable beyond those thresholds. Future work comparing how retinal circuits react across manipulations could distinguish among these possibilities. Finally, considering the transcriptional similarity between A_{OFF-T} and A_{OFF-S} ganglion cell types[15], differences in vulnerability of these two cell types across manipulations could be attributed to intrinsic properties not discernible by their transcriptomic profiles and/or by their extrinsic properties, i.e., input circuits.

Spatial and temporal adjustments following input loss found in cone-DTR retina demonstrate how functional homeostasis restores neuronal activity to a set point following perturbation. Homeostatic plasticity in the retina has been observed broadly: (1) potentiation of rod-to-rod bipolar cells in the rod degeneration *P23H* mice to maintain light sensitivity[36], (2) structural and functional compensation at second-order synapses upon partial loss of photoreceptors[20,21,37,38], (3) preserved cone-mediated light responses and fidelity of information transmission in a *CNGB1* model of rod degeneration[39], (4) maintained light responses in cones lacking outer segments in the rod degeneration *rd10* mouse[40,41], and (5) retained signal transmission and processing capacity of surviving circuitry in the rod degeneration *rd1* mouse[42]. Despite differences in the etiologies of photoreceptor death, these studies provide evidence that post-receptoral circuits can retain function during degeneration, which is consistent with our findings on functional adjustments that preserve perceptually relevant information within natural movies (Figure 8). The present observation of changes in temporal filters following partial cone loss emphasizes that such changes would be missed by conventional diagnostic tools for acuity which tend not to limit decision time for letter identification[43–45]. Such resiliency within the retina inspires efforts to develop (1) diagnostics sensitive to mild changes and (2) strategies to preserve surviving circuits to restore visual function. For example, computational models of morphologically accurate healthy and degenerated retina revealed maintained responsiveness of ON and OFF cone bipolar cells to electrical stimulation in degenerated retina[46]. Based on the resilience of cone vision, cone preservation would be a promising therapeutic strategy. However, further studies are required to determine the time window for effective intervention as a circuit's rewiring capacity, cone-mediated light responses, and visual behaviors all decline with age[37].

While our original findings suggested that the effects of partial cone loss could be interpreted as the entire retina sitting in a light adapted state[47], the present study demonstrates that retinal pathways undergo distinct functional and structural modifications. Maintenance of general center-surround receptive field structures and the fidelity of signaling despite input loss demonstrate compensatory changes that minimally degrade function. Such adaptive changes following input loss have been observed across sensory circuits. For example, in the auditory system, reduced input following noise-induced damage to the synapses of hair cells in the inner ear (cochlear synaptopathy) led to an increase in neural gain across a wide range of frequencies to compensate for input loss[48,49]. Similarly, acoustic trauma caused auditory cortical neurons to exhibit increased tone-evoked responses as a result of dynamic properties of inhibition, which led to the expansion of receptive fields[50]. Another study reported the recovery of functional patterns of auditory cortical activity potentially via changes in the balance of excitatory and inhibitory inputs in adult-onset deafness[1]. Across the auditory and visual systems, inhibitory neurons exhibit greater dynamics than excitatory neurons[2,3]. For example, in the visual system, greater flexibility of inhibitory circuits were found both in the visual cortex and in the retina as reported here[21]. Even beyond pathways within one sensory system, robust plasticity in the form of cortical reorganization has been observed in compensation across sensory modalities in the mature nervous system[51–54].

Previous studies have shown that neurons exhibit different vulnerability and plasticity upon deafferentation[1–4,15–18], but how each cell type responds and where these changes occur within the circuits have not been examined. By investigating spatiotemporal properties of two different types of A_{OFF} ganglion cells, we demonstrate unique outcomes in response to common input loss and provide mechanistic insights on those changes across recording configuration through pharmacology. Moreover, we assessed the consequences of changes in spatiotemporal processing on visual perception of natural movies, which incorporates a dimension beyond previous assessments of static natural scenes.

ACKNOWLEDGEMENTS

We thank Annika Balraj, Jonah Chan, Jeanette Hyer, Yvonne Ou, Rachel O.L. Wong for helpful discussions and comments. This work was supported by NIH through the Vision Core Grants P30 EY002162 (UCSF), K99EY033858 (J.Y.L) and EY029772 (F.A.D.) and by foundation grants from McKnight Scholar Award, Research to Prevent Blindness Unrestricted Grant, and All May See.

AUTHOR INFORMATION

Contributions

Conceptualization, methodology, software, resources, writing – review & editing, J.Y.L., D.B.K, S.C.H, and F.A.D.; formal analysis, J.Y.L., D.B,K, S.C.B, L.D.S., J.V.J., and F.A.D.; investigation, visualization, J.Y.L. and F.A.D.; data curation; J.Y.L., D.B,K.; validation, writing – original draft, supervision, project administration, funding acquisition, J.Y.L. and F.A.D.

ONLINE METHODS

Mice

All procedures were done in accordance with the University of California, San Francisco Institutional Animal Care and Use protocols. Animals were maintained on a 12 h dark-12 h light cycle and fed standard mouse diet ad libitum. The following transgenic mouse lines were crossed: *OPN1MWCre* (Le et al., 2004) for Cre-recombinase expression in cones expressing middle wavelength sensitive (M)-opsin, with *Rosa26-loxP-stop-loxP-DTR* (Buch et al., 2005) for Cre-dependent expression of diphtheria toxin receptor (DTR). All transgenic mice were backcrossed into the C57BL/6J background. Male and female mice were used for experiments.

Diphtheria toxin induced cone death

To induce cone death, one intramuscular diphtheria toxin injection was made between P30-40 at a dosage between 50 ng/g and 75 ng/g for OPN1MW-Cre[20,21]. Dosages were adjusted to induce approximately 50% cone loss. DTR-negative littermates were used as control and injected with an equivalent volume of saline. Experiments were performed within 55 days after the injection. We did not find significant changes to spatiotemporal properties across the shorter and longer halves of the interval.

Tissue preparation for immunostaining

Immunostaining protocols were identical to those described previously[20,21]. Specific reagents used in this study are listed in the Key Resources Table.

Image acquisition

Type 2 and 3a OFF bipolar cells and their associated synaptic puncta were imaged on a Leica SP8 confocal microscope using a 40x 1.3 numerical aperture (NA) oil-immersion objective. Image stacks were acquired with a voxel size of 0.09 µm (x axis, y axis) and 0.3 µm (z axis).

Each plane was acquired 2 times to obtain the average. Individual dye-filled A_{OFF-S} and A_{OFF-T} ganglion cells were localized using epifluorescence and their dendrites and associated synaptic puncta were imaged with the following settings: 40x (1.3 NA) objective at resolution of 0.102 x 0.102 x 0.3 µm. A_{OFF-S} and A_{OFF-T} ganglion cells were identified by stratification level of their dendrites[55].

Electrophysiology tissue preparation

Procedures for patch-clamp recording of A_{OFF-S} and A_{OFF-T} ganglion cells in flat mount retina were identical to those described previously[20,21,38]. For bar noise stimuli (Figures 1-7), recordings were made in dorsal-nasal retina where the largest A-type ganglion cells reside[56] and where middle (M)-wavelength sensitive opsin dominates[57]. Following recordings, retinas were mounted on filter paper, fixed in 2% paraformaldehyde for 15-20 min, and processed for immunostaining.

Patch-clamp recordings

Patch-clamp recordings from ganglion cells were identical to those described previously[21]. Patch electrodes were pulled from borosilicate glass (Sutter instruments) on a Narishige puller to 3–6 MOhm resistance. Under infrared light (950 nm), large round somas were targeted as putative A_{OFF-S} ganglion cells and large oblong somas were targeted as putative A_{OFF-T} ganglion cells. To type cells, extracellular spikes were recorded with an electrode filled with HEPES-buffered Ames in cell-attached configuration. A_{OFF-S} ganglion cells were identified by their characteristically sustained spiking before and after a 500 ms light increment. A_{OFF-T} ganglion cells were identified by their characteristically transient spiking after a 500 ms light increment. Once the the ganglion cell was identified, a new electrode was used to make an intracellular recording. Whole-cell recordings were made with an electrode filled with internal solution containing either potassium aspartate for current-clamp recordings (Figures 1I, 3I-N, 5I-N, 6, S3H-I) or cesium methane sulfonate for voltage-clamp recordings when acquired in the same cell (Figures 1J, 2, 3C-E, 4, 5C-H, 7, S3G, S4) and 0.04% Lucifer yellow dye[20,21]. Voltage-clamp recordings were made before and after the application of 100µM picrotoxin and 5µM strychnine (Figures 2, 4, 7). For perforated patch-clamp recordings in Figure S6, amphotericin-B (0.05 mg/ml) was added to the potassium aspartate internal solution in the back portion, but not the front tip, of the electrode to allow a delay before perforating the cell membrane[21,38].

Light stimuli

To elicit spike responses for cell identification, a 470 nm LED was used to deliver a uniform spot 2000 μm in diameter for 500 ms. This wavelength was used to preferentially stimulate rods between the ranges of 8–400 photoisomerizations per rod per sec (Rh*/rod/sec). Procedures for measuring the spatiotemporal receptive field profiles were identical to those described previously[21]. To preferentially elicit cone-mediated responses, we presented flickering bars with intensities drawn from a Gaussian white noise distribution with mean intensity of 8,400 Rh*/rod/sec to adapt rods[20,21].

Intrinsic excitability of OFF ganglion cells

For current injection experiments (Figure S6A-F), procedures were identical to those described in Lee et al. 2022[21]. Spike threshold and resting membrane potential were calculated by injecting a slow ramp of current (Figure S6G-H). Resting membrane potential was taken as the initial membrane voltage 500ms before injecting a linear current injection ramp from 0 to 300pA and spike threshold was the average voltage at which a cell initiated its first action potential in response to the ramp.

Quantification of cone numbers

Procedure for counting cones, labeled either by cone arrestin or peanut agglutinin, were identical to those described previously[20,21].

Quantification of synaptic density

To quantify synaptic puncta associated with specific cell types, we used confocal images of type 2 and 3a bipolar cells labeled by immunostaining for Syt2 and HCN4 in the OFF sublamina, respectively, and individual ganglion cells filled with Lucifer Yellow during physiology experiments. ImageJ was used to median filter the images to remove thermal noise generated by the microscope's detectors. We created a binary mask of bipolar cell axons of interest (Amira) and VolumeCut was used to select the OFF sublamina labeling of Syt2 and HCN4 within the IPL. Synaptic puncta associated with bipolar cell axons, $A_{OFF\text{-}S}$ and $A_{OFF\text{-}T}$ ganglion cell dendrites were identified and manually validated in ObjectFinder with methods previously used[21,58]. Puncta distribution of PSD95, GlyRα1, and $GABA_A$β2,3 within the dendrites of individual $A_{OFF\text{-}S}$ and $A_{OFF\text{-}T}$ ganglion cells were identified and quantified using ObjectFinder. Imaris was used to generate a 3-dimensional dendritic skeleton of the ganglion cell. Custom-written MATLAB routines were used to create a binary mask and used as a criteria to include CtBP2, GlyRα1, and $GABA_A$β2,3 that exceeds 50% overlap with a mask. Linear puncta

density was calculated within a moving window of 10 μm along the dendritic skeleton, starting from the cell soma.

Linear-nonlinear model

Procedures for analyzing spatiotemporal receptive fields of spikes, subthreshold voltages, excitatory, and inhibitory currents were identical to those described previously[21]. As in the previous work, we normalized the linear filter such that it was a unit vector. This choice of normalization places all gain information into the nonlinearity. In response to the bar stimulus, the linear filter was used to measure temporal information. A single temporal linear filter was measured by projecting the linear filters from each region of space along the first principal component measured across all filters. A single spatial filter was measured by projecting the linear filters across time along the first principal component across filters. The nonlinear component of the model maps the convolution of the linear filter and stimulus to the cell's response, i.e., spikes, voltage, excitatory current, or inhibitory current (Figures 5-6).

The linear-nonlinear model was also used in the current injection analysis (Figures S6A-F). The time-reversed spike-triggered average of the injected current represents the linear filter. The nonlinear filter is plotted with the abscissa as the convolution between the spike-triggered average and the stimulus in units of standard deviation against the ordinate, which is the spike rate (Figure S6B). The nonlinearity for each cell was interpolated and smoothed with a spline function before calculating the average.

Principal components analysis

The temporal filters (Figure 1), spatial filters (Figure 3), or the nonlinearities (Figure 5) were plotted across conditions (i.e., control, cone-DTR, and partial stimulation for $A_{OFF\text{-}S}$ and $A_{OFF\text{-}T}$ ganglion cells) in n-dimensional space, where n is the number of points in the linear filters or nonlinearities. Before running PCA, the spatial filters were aligned to their centers. To compare the impact on cone loss nonlinearities of inputs vs. outputs (Figure 6), nonlinearities were plotted across recording configurations for either $A_{OFF\text{-}S}$ or $A_{OFF\text{-}T}$ ganglion cells. For the pharmacological manipulations, a difference filter was calculated between the temporal (or spatial) filters and nonlinearities before and after the application of the antagonist. Average differences were for display purposes only (Figures 2, 4, 7F, J, O, S). Differences calculated for each individual cell before and after pharmacological manipulations were used for the actual analysis. For both the individual and the difference filters and nonlinearities the

dimension of maximum variance was found across conditions, and that vector was assigned the first principal component (PC1). The magnitude of the projection onto the first principal component was compared between conditions: control vs. cone-DTR, control vs. partial, and cone-DTR vs. partial. The results of these comparisons were used in conjunction to assign mechanisms (Figure 1B-E).

Mean difference vector analysis

In the cases where the first principal component was found to be significantly different between control vs. cone-DTR conditions, we parameterized the filters to determine which characteristics contributed most to the observed changes (Figure S2F-H). For temporal filters, we used the following features: time to peak, time to trough, peak amplitude, trough amplitude, and time to zero crossing (Figure 1L-O). For spatial filters, we used the following features: center height, surround height, center width, and surround width (Figure 3L-N). Each filter, whether temporal or spatial, was represented as a point in n-dimensional space, where n is the number of observations (across space or time) within the filter. For each control filter, we then measured the extent to which modifying each feature changed the filter to become more or less like the mean cone DTR filter. This was done by linearly modifying the control filter, and then projecting that modified filter onto the n-dimensional vector that pointed from the mean control filter to the mean cone DTR filter ("mean difference vector", representing the direction in n-dimensional space that one must travel to go from the average control filter to the average cone DTR filter; Figure S2F-H). For example, if time to peak shifted under cone loss conditions, we created a temporal filter reflecting that degree of change for each control filter, and then projected the positions of these modified filters onto the mean difference vector. The projection values were normalized such that 1.0 corresponded to the position of the mean cone DTR filter and 0.0 corresponded to the position of the mean control filter. Thus, the closer a projection was to 1.0, the more that particular feature modification shifted the filter in the direction of cone DTR filters. This analysis was repeated for each combination of feature modifications, and the mean marginal contribution of each feature was computed across all combinations to reveal the final contribution values. Because not all features were necessarily independent, it was possible to achieve values outside the interval of [0.0, 1.0].

Quantification of movie similarity

Spatial receptive fields were generated by revolving the average linear spatial filters from control, cone-DTR and partial stimulation of control retinas. For each time point of the temporal

receptive field, the corresponding spatial receptive field was calculated to form a 3D spatio-temporal receptive field. 3D convolution was applied to the movie frames using the 3D spatio-temporal receptive field to produce the filtered output movies for each condition. Such a convolution was done on 6 natural scene movies from Freiheit, 2016[59]. The movie was converted to grayscale and segmented into multiple pieces, each lasting 5 to 10 seconds. 3D spatio-temporal receptive field sizes were scaled to convolve a reference movie across a range of resolutions: 15.42, 18.46, 160, and 640 times the receptive field pixel size. In mice, each degree of the visual field corresponds to about 31μm of the retina[60,61]. Given that the receptive field sizes of alpha ganglion cells are about 300μm, which gives us 10 degrees/receptive field, and each monocular visual field spans roughly 180 degrees[62]. The mean squared error (MSE, non-perceptual similarity index) and structural similarity index (SSIM, perceptual similarity index) were used to quantify the difference between convolved movies with the reference movies as a function of movie-to-receptive field pixel ratios. MSE and SSIM across movie-to-receptive field pixel ratios are shown in Figure S7. For each frame of the movie, SSIM and MSE were calculated and the average value was reported. Procedure for analyzing static image similarity were identical to those described previously[21].

Statistical analysis

Data are represented as median ± interquartile range (IQR) in Figures 1I-J, 2H, 2L, 2Q, 2U, 3C-D, 3F-G, 3I-J, 4H, 4L, 4Q, 4U, 5C-D, 5F-G, 5I-J, 5L-M, 7H, 7L, 7Q, 7U, S2C-D, S3C-D, S3G-H, S4A-B, S5B-G, S5I-L, as mean ± sem in Figures 8C-H, and S7, and as median ± propagated error in Figures 1L, 2I, 2M, 2R, 2V, 3E, 3H, 3K, 4I, 4M, 4R, 4V, 5E, 5H, 5K, 5N, 6E-H, 6M-P, 7I, 7M, 7R, 7V, S2E, S3E, S3I, S4C. A Wilcoxon rank-sum test (abbr. rank sum) with Bonferroni-Holm method was used to determine significant differences across the three conditions. A permutation test with Bonferroni-Holm method was used for Figures 1L, 2I, 2M, 2R, 2V, 3E, 3H, 3K, 4I, 4M, 4R, 4V, 5E, 5H, 5K, 5N, 6E-H, 6M-P, 7I, 7M, 7R, 7V. A two-way ANOVA test was used to determine significant differences between convolved movies [or images] with the reference movies [or images] (Figures 8 and S7). The following asterisks in the figures indicate p values: * ≤ 0.05, ** ≤ 0.01, *** ≤ 0.005.

REAGENT or RESOURCE	SOURCE	IDENTIFIER
Antibodies		

Rabbit polyclonal anti-cone arrestin	Millipore	Cat# AB15282; RRID:AB_1163387
Mouse monoclonal anti-gephyrin	Synaptic System	Cat# 147 111: RRID: AB_887719
Mouse polyclonal anti-$GABA_A$Rβ2,3	Millipore	Cat# MAB341: RRID: AB_2109419
Mouse polyclonal anti-GlyRα1	Synaptic System	Cat# 146111: RRID: AB_887723
Mouse monoclonal anti-synaptotagmin II (Syt2)	Zebrafish International resource center	Cat# znp-2: RRID: AB_10013783
Rabbit polyclonal anti-HCN4	Alomone Labs	Cat# APC-052: RRID: AB_2039906
Rabbit polyclonal anti-Lucifer Yellow	Life Technologies	Cat# A-5750: RRID: AB_2536190
Mouse monoclonal anti-CtBP2	BD Bioscience	Cat# 612044: RRID: AB_399431
Donkey polyclonal anti-mouse-Dylight 405	Jackson Immunoresearch	Cat# 715-475-150; RRID:AB_2340839
Donkey polyclonal anti-mouse-Alexa 647	Jackson Immunoresearch	Cat# 715-605-151; RRID:AB_2340863
Donkey polyclonal anti-rabbit-Alexa 488	Jackson Immunoresearch	Cat# 711-545-152; RRID:AB_2313584
Chemicals, Peptides, and Recombinant Proteins		
Normal Donkey Serum	Jackson Immunoresearch	Cat# NC9624464
Ames' Medium	United States Biological	Cat# A1372-25
Vectashield	Vector Laboratories	Cat# H-1000; RRID: AB_2336789
Picrotoxin	Thermo Fischer Scientific	P1675-1G
Strychnine	Sigma-Aldrich	S8753

Experimental Models: Organisms/Strains		
Mouse model: *C57BL/6-Gt(ROSA)26Sortm1(HBEGF)Awai/J (DTR)*	The Jackson Laboratory	Cat# JAX:007900; RRID:IMSR_JAX:007900
Mouse model: *OPNMW1-Cre (HRGP-Cre)*	Le et al., 2004[63]	N/A
Software and Algorithms		
ImageJ	NIH	https://imagej.nih.gov/ij/, RRID: SCR_003070
Amira	Thermo-Fisher Scientific	https://www.fei.com/software/amira-avizo/, RRID: SCR_014305
Imaris	Bitplane	http://www.bitplane.com/, RRID: SCR_007370
Matlab	Mathworks	https://www.mathworks.com/products/matlab.html, RRID: SCR_001622
Igor Pro	Igor Pro	RRID:SCR_000325
Object Finder	Della Santina et al. 2013[64]	https://github.com/lucadellasantina/ObjectFinder http://doi.org/10.5281/zenodo.4767847
VolumeCut	Della Santina et al. 2021[65]	https://github.com/lucadellasantina/VolumeCut http://doi.org/105281/zenodo.5048331
Symphony and Stage	Mark Cafaro and Fred Rieke	https://github.com/Symphony-DAS/symphony-v1/wiki https://github.com/Stage-VSS/stage-v1
Natural Movies	Freiheit, 2016[59]	https://www.youtube.com/watch?v=Foi3Hblg21s

ETHICS DECLARATIONS

The authors declare no competing interests.

DATA AVAILABILITY

- All data reported in this paper will be shared by the lead contacts upon request.

- Any additional information required to reanalyze the data reported in this paper is available from the lead contact upon request.

CODE AVAILABILITY

- All original code for the image analysis has been deposited at Github and is publically available as of the date of publication. The information is listed in the key resources table.

SUPPLEMENTAL INFORMATION

Document S1. Figures S1-S7 and Tables S1-S8.

REFERENCES

1. Karoui, C. *et al.* Auditory cortical plasticity after cochlear implantation in asymmetric hearing loss is related to spatial hearing: a PET H215O study. *Cereb. Cortex* 33, 2229–2244 (2023).
2. Villa, K. L. *et al.* Inhibitory Synapses Are Repeatedly Assembled and Removed at Persistent Sites In Vivo. *Neuron* 89, 756–769 (2016).
3. Eavri, R. *et al.* Interneuron Simplification and Loss of Structural Plasticity As Markers of Aging-Related Functional Decline. *J. Neurosci.* 38, 8421–8432 (2018).
4. Kumar, M. *et al.* Cell-type-specific plasticity of inhibitory interneurons in the rehabilitation of auditory cortex after peripheral damage. *Nat. Commun.* 14, 4170 (2023).
5. Liu, Y. *et al.* Piriform cortical glutamatergic and GABAergic neurons express coordinated plasticity for whisker-induced odor recall. *Oncotarget* 8, 95719–95740 (2017).
6. Shekhar, K. *et al.* Comprehensive Classification of Retinal Bipolar Neurons by Single-Cell Transcriptomics. *Cell* 166, 1308-1323.e30 (2016).
7. Baden, T. *et al.* The functional diversity of retinal ganglion cells in the mouse. *Nature* 529, 345–350 (2016).
8. Puthussery, T., Gayet-Primo, J., Pandey, S., Duvoisin, R. M. & Taylor, W. R. Differential loss and preservation of glutamate receptor function in bipolar cells in the rd10 mouse model of

retinitis pigmentosa. *Eur. J. Neurosci.* 29, 1533–1542 (2009).

9. Murphy, G. J. & Rieke, F. Network Variability Limits Stimulus-Evoked Spike Timing Precision in Retinal Ganglion Cells. *Neuron* 52, 511–524 (2006).
10. Eggers, E. D., McCall, M. A. & Lukasiewicz, P. D. Presynaptic inhibition differentially shapes transmission in distinct circuits in the mouse retina. *J. Physiol.* 582, 569–582 (2007).
11. Chichilnisky, E. J. & Kalmar, R. S. Functional Asymmetries in ON and OFF Ganglion Cells of Primate Retina. *J. Neurosci.* 22, 2737–2747 (2002).
12. Kim, K. J. & Rieke, F. Temporal Contrast Adaptation in the Input and Output Signals of Salamander Retinal Ganglion Cells. *J. Neurosci.* 21, 287–299 (2001).
13. Chander, D. & Chichilnisky, E. J. Adaptation to temporal contrast in primate and salamander retina. *J. Neurosci. Off. J. Soc. Neurosci.* 21, 9904–9916 (2001).
14. Nirenberg, S., Bomash, I., Pillow, J. W. & Victor, J. D. Heterogeneous response dynamics in retinal ganglion cells: the interplay of predictive coding and adaptation. *J. Neurophysiol.* 103, 3184–3194 (2010).
15. Tran, N. M. *et al.* Single-Cell Profiles of Retinal Ganglion Cells Differing in Resilience to Injury Reveal Neuroprotective Genes. *Neuron* 104, 1039-1055.e12 (2019).
16. Ou, Y., Jo, R. E., Ullian, E. M., Wong, R. O. L. & Della Santina, L. Selective Vulnerability of Specific Retinal Ganglion Cell Types and Synapses after Transient Ocular Hypertension. *J. Neurosci. Off. J. Soc. Neurosci.* 36, 9240–9252 (2016).
17. Wang, A. Y. M. *et al.* Retinal ganglion cell dysfunction in mice following acute intraocular pressure is exacerbated by P2X7 receptor knockout. *Sci. Rep.* 11, 4184 (2021).
18. O'Brien, E. E., Greferath, U. & Fletcher, E. L. The effect of photoreceptor degeneration on ganglion cell morphology: Ganglion cells in retinal degeneration. *J. Comp. Neurol.* 522, 1155–1170 (2014).
19. Hahn, J. *et al.* Evolution of neuronal cell classes and types in the vertebrate retina. *Nature* 624, 415–424 (2023).

20. Care, R. A. *et al.* Partial Cone Loss Triggers Synapse-Specific Remodeling and Spatial Receptive Field Rearrangements in a Mature Retinal Circuit. *Cell Rep.* 27, 2171-2183.e5 (2019).
21. Lee, J. Y., Care, R. A., Kastner, D. B., Della Santina, L. & Dunn, F. A. Inhibition, but not excitation, recovers from partial cone loss with greater spatiotemporal integration, synapse density, and frequency. *Cell Rep.* 38, 110317 (2022).
22. Enroth-Cugell, C. & Freeman, A. W. The receptive-field spatial structure of cat retinal Y cells. *J. Physiol.* 384, 49–79 (1987).
23. Atick, J. J. & Redlich, A. N. Towards a Theory of Early Visual Processing. *Neural Comput.* 2, 308–320 (1990).
24. Fox, M. A. & Sanes, J. R. Synaptotagmin I and II are present in distinct subsets of central synapses. *J. Comp. Neurol.* 503, 280–296 (2007).
25. Yu, W.-Q. *et al.* Synaptic Convergence Patterns onto Retinal Ganglion Cells Are Preserved despite Topographic Variation in Pre- and Postsynaptic Territories. *Cell Rep.* 25, 2017-2026.e3 (2018).
26. Ichinose, T. & Hellmer, C. B. Differential signalling and glutamate receptor compositions in the OFF bipolar cell types in the mouse retina. *J. Physiol.* 594, 883–894 (2016).
27. Awatramani, G. B. & Slaughter, M. M. Origin of transient and sustained responses in ganglion cells of the retina. *J. Neurosci. Off. J. Soc. Neurosci.* 20, 7087–7095 (2000).
28. DeVries, S. H. Bipolar Cells Use Kainate and AMPA Receptors to Filter Visual Information into Separate Channels. *Neuron* 28, 847–856 (2000).
29. Asari, H. & Meister, M. Divergence of visual channels in the inner retina. *Nat. Neurosci.* 15, 1581–1589 (2012).
30. Franke, K. *et al.* Inhibition decorrelates visual feature representations in the inner retina. *Nature* 542, 439–444 (2017).
31. Graydon, C. W. *et al.* Synaptic Transfer between Rod and Cone Pathways Mediated by AII

Amacrine Cells in the Mouse Retina. *Curr. Biol. CB* 28, 2739-2751.e3 (2018).

32. Nieuwenhuis, S., Forstmann, B. U. & Wagenmakers, E.-J. Erroneous analyses of interactions in neuroscience: a problem of significance. *Nat. Neurosci.* 14, 1105–1107 (2011).
33. Wang, Z., Bovik, A. C., Sheikh, H. R. & Simoncelli, E. P. Image quality assessment: from error visibility to structural similarity. *IEEE Trans. Image Process. Publ. IEEE Signal Process. Soc.* 13, 600–612 (2004).
34. Gogliettino, A. R. *et al.* High-Fidelity Reproduction of Visual Signals by Electrical Stimulation in the Central Primate Retina. *J. Neurosci.* 43, 4625–4641 (2023).
35. Sinha, R. *et al.* Transient expression of a GABA receptor subunit during early development is critical for inhibitory synapse maturation and function. *Curr. Biol.* 31, 4314-4326.e5 (2021).
36. Leinonen, H. *et al.* Homeostatic plasticity in the retina is associated with maintenance of night vision during retinal degenerative disease. *eLife* 9, e59422 (2020).
37. Shen, N., Wang, B., Soto, F. & Kerschensteiner, D. Homeostatic Plasticity Shapes the Retinal Response to Photoreceptor Degeneration. *Curr. Biol.* 30, 1916-1926.e3 (2020).
38. Care, R. A. *et al.* Mature Retina Compensates Functionally for Partial Loss of Rod Photoreceptors. *Cell Rep.* 31, 107730 (2020).
39. Scalabrino, M. L. *et al.* Robust cone-mediated signaling persists late into rod photoreceptor degeneration. *eLife* 11, e80271 (2022).
40. Ellis, E. M. *et al.* Cones and cone pathways remain functional in advanced retinal degeneration. *Curr. Biol. CB* 33, 1513-1522.e4 (2023).
41. Xu, H. *et al.* Visual pigment-deficient cones survive and mediate visual signaling despite the lack of outer segments. *Proc. Natl. Acad. Sci. U. S. A.* 119, e2115138119 (2022).
42. Rodgers, J. *et al.* Functional integrity of visual coding following advanced photoreceptor degeneration. *Curr. Biol. CB* 33, 474-486.e5 (2023).

43. Ratnam, K., Carroll, J., Porco, T. C., Duncan, J. L. & Roorda, A. Relationship Between Foveal Cone Structure and Clinical Measures of Visual Function in Patients With Inherited Retinal Degenerations. *Investig. Opthalmology Vis. Sci.* 54, 5836 (2013).

44. Foote, K. G. *et al.* Relationship Between Foveal Cone Structure and Visual Acuity Measured With Adaptive Optics Scanning Laser Ophthalmoscopy in Retinal Degeneration. *Invest. Ophthalmol. Vis. Sci.* 59, 3385–3393 (2018).

45. Ferris, F. L., Kassoff, A., Bresnick, G. H. & Bailey, I. New visual acuity charts for clinical research. *Am. J. Ophthalmol.* 94, 91–96 (1982).

46. Farzad, S. *et al.* Impact of Retinal Degeneration on Response of ON and OFF Cone Bipolar Cells to Electrical Stimulation. *IEEE Trans. Neural Syst. Rehabil. Eng. Publ. IEEE Eng. Med. Biol. Soc.* 31, 2424–2437 (2023).

47. Lee, J. Y., Care, R. A., Della Santina, L. & Dunn, F. A. Impact of Photoreceptor Loss on Retinal Circuitry. *Annu. Rev. Vis. Sci.* 7, 105–128 (2021).

48. Monaghan, J. J. M., Garcia-Lazaro, J. A., McAlpine, D. & Schaette, R. Hidden Hearing Loss Impacts the Neural Representation of Speech in Background Noise. *Curr. Biol.* 30, 4710-4721.e4 (2020).

49. Barbour, D. L. Hidden Hearing Loss: Mixed Effects of Compensatory Plasticity. *Curr. Biol.* 30, R1433–R1436 (2020).

50. Scholl, B. & Wehr, M. Disruption of Balanced Cortical Excitation and Inhibition by Acoustic Trauma. *J. Neurophysiol.* 100, 646–656 (2008).

51. Petrus, E. *et al.* Crossmodal induction of thalamocortical potentiation leads to enhanced information processing in the auditory cortex. *Neuron* 81, 664–673 (2014).

52. Jitsuki, S. *et al.* Serotonin mediates cross-modal reorganization of cortical circuits. *Neuron* 69, 780–792 (2011).

53. Ewall, G., Parkins, S., Lin, A., Jaoui, Y. & Lee, H.-K. Cortical and Subcortical Circuits for Cross-Modal Plasticity Induced by Loss of Vision. *Front. Neural Circuits* 15, 665009 (2021).

54. Kral, A. & Sharma, A. Crossmodal plasticity in hearing loss. *Trends Neurosci.* 46, 377–393 (2023).

55. Krieger, B., Qiao, M., Rousso, D. L., Sanes, J. R. & Meister, M. Four alpha ganglion cell types in mouse retina: Function, structure, and molecular signatures. *PloS One* 12, e0180091 (2017).

56. Sawant, A. *et al.* Organization and emergence of a mixed GABA-glycine retinal circuit that provides inhibition to mouse ON-sustained alpha retinal ganglion cells. *Cell Rep.* 34, 108858 (2021).

57. Applebury, M. L. *et al.* The murine cone photoreceptor: a single cone type expresses both S and M opsins with retinal spatial patterning. *Neuron* 27, 513–523 (2000).

58. Della Santina, L., Inman, D. M., Lupien, C. B., Horner, P. J. & Wong, R. O. L. Differential Progression of Structural and Functional Alterations in Distinct Retinal Ganglion Cell Types in a Mouse Model of Glaucoma. *J. Neurosci.* 33, 17444–17457 (2013).

59. *GoPro Awards: Squirrel Runs Off With GoPro*. (2016).

60. Remtulla, S. & Hallett, P. E. A schematic eye for the mouse, and comparisons with the rat. *Vision Res.* 25, 21–31 (1985).

61. Schmucker, C. & Schaeffel, F. A paraxial schematic eye model for the growing C57BL/6 mouse. *Vision Res.* 44, 1857–1867 (2004).

62. Scholl, B., Burge, J. & Priebe, N. J. Binocular integration and disparity selectivity in mouse primary visual cortex. *J. Neurophysiol.* 109, 3013–3024 (2013).

63. Le, Y.-Z. *et al.* Targeted expression of Cre recombinase to cone photoreceptors in transgenic mice. *Mol. Vis.* 10, 1011–1018 (2004).

64. Della Santina, L., Inman, D. M., Lupien, C. B., Horner, P. J. & Wong, R. O. L. Differential Progression of Structural and Functional Alterations in Distinct Retinal Ganglion Cell Types in a Mouse Model of Glaucoma. *J. Neurosci.* 33, 17444–17457 (2013).

65. Della Santina, L. *et al.* Disassembly and rewiring of a mature converging excitatory circuit

following injury. *Cell Rep.* 36, 109463 (2021).

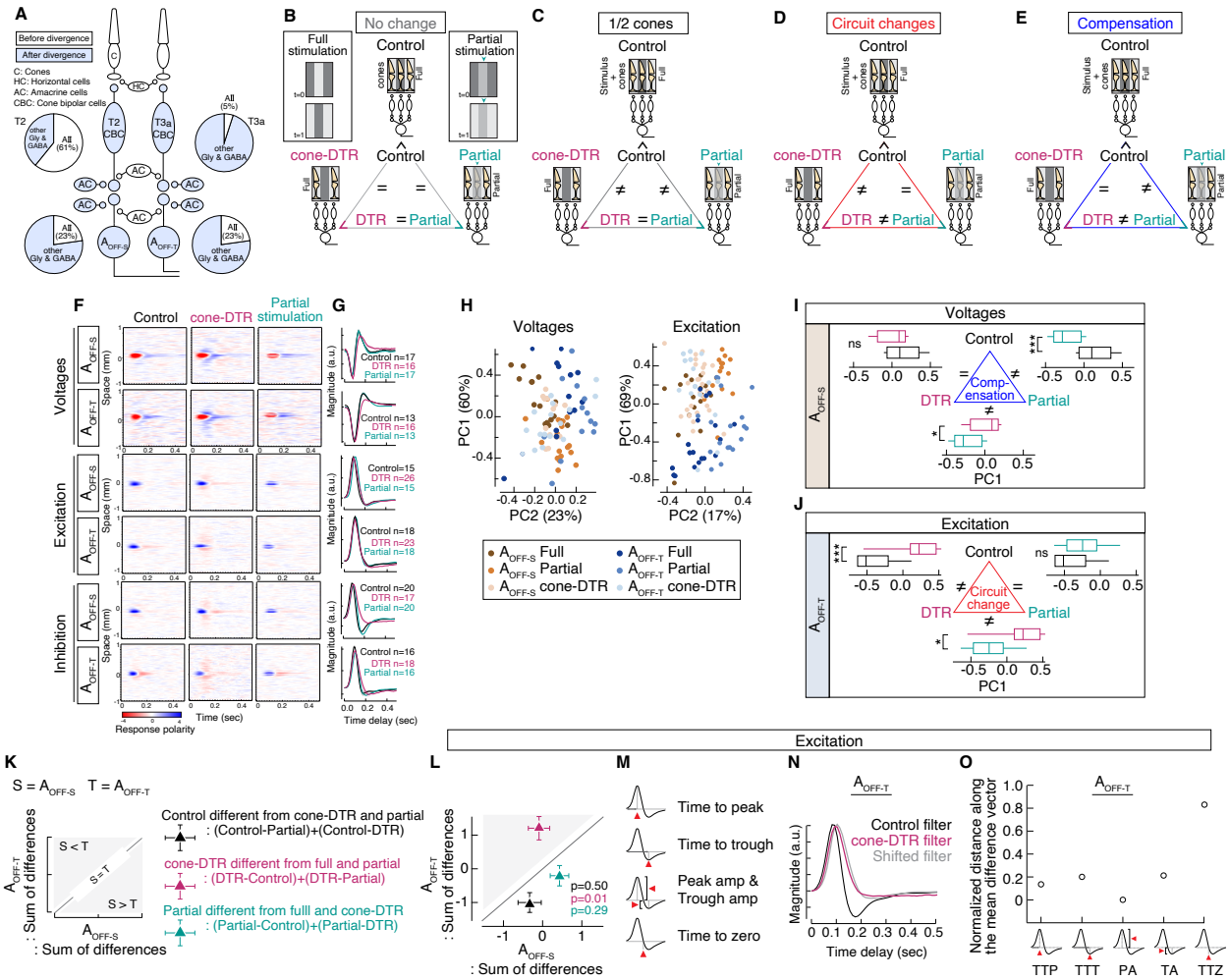

Figure 1. Partial cone loss causes differential temporal changes to A_{OFF} ganglion cell types. (A) Illustration of known cone pathways to $A_{OFF\text{-}S}$ and $A_{OFF\text{-}T}$ ganglion cells. Cones contact type 2 (T2) and 3a (T3a) OFF cone bipolar cells (CBCs), which receive different degrees of inhibitory inputs from AII and other amacrine cell types (top pie charts). T2 and T3a CBCs primarily contact $A_{OFF\text{-}S}$ and $A_{OFF\text{-}T}$ ganglion cells, respectively. Each ganglion cell type receives glycinergic and GABAergic inhibitory inputs and equivalent contributions from AII amacrine cells (bottom pie charts). If cone ablation affects circuits before divergence of the OFF pathways, then the following sites are implicated (white): cones, horizontal cells, common amacrine cells. If cone ablation affects circuits after divergence of the OFF channels, then the following locations are implicated (blue): bipolar cells (T2 or T3a), different amacrine cells that send their inputs to sustained or transient pathways. (B-E) Comparison of three conditions and their state of cones and the retinal circuit: (1) control condition has a full complement of cones and a control circuit (control); (2) DTR condition has half the cones and a DTR circuit (cone-DTR); (3) half stimulation condition has stimulation of half the cones and a control circuit (partial). Triangles represent comparisons among three conditions that would be interpreted as (B) no change, mechanisms caused by (C) half cone stimulation, (D) circuit changes, or (E) compensation. (F) Example spatio-temporal filters in response to a bar noise stimulus under three conditions for either $A_{OFF\text{-}S}$ (rows 1, 3, 5) or $A_{OFF\text{-}T}$ (rows 2, 4, 6) under current clamp for measuring voltages (rows 1-2), voltage clamp for measuring excitation (rows 3-4) or inhibition (rows 5-6). (G) Average temporal filters of (odd rows) $A_{OFF\text{-}S}$ and (even rows) $A_{OFF\text{-}T}$ ganglion cells measuring voltages (rows 1-2), excitation (rows 3-4), and inhibition (rows 5-6) for control

(black), cone-DTR (magenta) and partial stimulation (green). (H) Each temporal filter is plotted as a function of its projection onto the first and second principal components from voltages (left) and excitation (right). Variance captured by each principal component noted on the corresponding axis. $A_{OFF\text{-}S}$ plotted in warm colors and $A_{OFF\text{-}T}$ plotted in cool colors for the three conditions. (I-J) Box plots of first principal components (PC1) for each pairwise comparison of conditions for (I) $A_{OFF\text{-}S}$ ganglion cell voltages and (J) $A_{OFF\text{-}T}$ ganglion cell excitation. Interpretation of mechanisms in the triangle center. (K) Schematic represents sum of differences for PC1 (see equations, right) for distinguishing whether each of the conditions is significantly different than the other two conditions: control (black), cone-DTR (magenta), and partial (green) for $A_{OFF\text{-}S}$ (abscissa) and $A_{OFF\text{-}T}$ (ordinate) ganglion cells. (L) Comparison of sum of differences between $A_{OFF\text{-}S}$ and $A_{OFF\text{-}T}$ ganglion cells for the projection onto excitatory PC1. Gray regions indicate where a significant difference was found. (M) Features extracted from temporal filters: time to peak (TTP), time to trough (TTT), peak amplitude (PA), trough amplitude (TA), and time to zero crossing (TTZ). (N) Average temporal filters under control and cone-DTR conditions for $A_{OFF\text{-}T}$ ganglion cells, which show a significant difference, and a version of the control temporal filter shifted by multiple features to match the cone-DTR temporal filter. (O) Normalized distance between the temporal filter in control (ordinate = 0) and cone-DTR (ordinate = 1) when the control temporal filter is changed by each feature. P-values in box plots indicate rank sum comparison between each pair of conditions after correcting for multiple comparisons with the Bonferroni-Holm method (I-J). P-values in scatter plot (L) indicate significant differences between $A_{OFF\text{-}S}$ and $A_{OFF\text{-}T}$ ganglion cells from a permutation test with correction for multiple comparisons. The following asterisks indicate p values: * ≤ 0.05, ** ≤ 0.01, *** ≤ 0.005. See also Figures S2 and S3; Table S1.

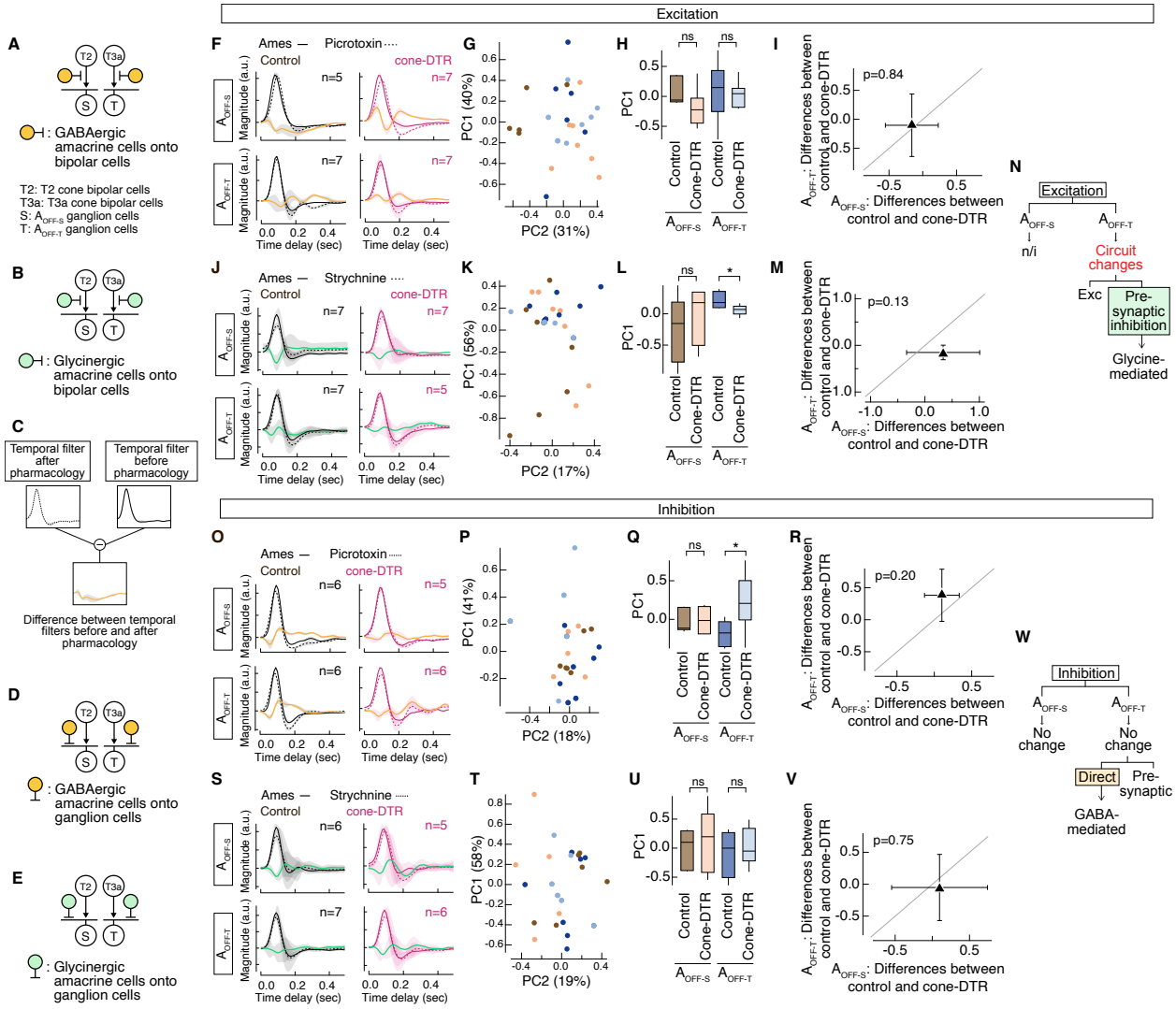

Figure 2. Partial cone loss causes presynaptic glycine and direct GABA inhibition to mediate changes in the cone-DTR temporal filters of $A_{OFF\text{-}T}$ ganglion cells. (A-B, D-E) Schematic of retinal pathways leading to the $A_{OFF\text{-}S}$ (left) and $A_{OFF\text{-}T}$ (right) ganglion cells and the circuit motifs for direct excitation (white), presynaptic inhibition from (A) GABA (yellow) or (B) glycine (green), and direct inhibition from (D) GABA (yellow) or (E) glycine (green) that would be blocked by (A, D) picrotoxin, an antagonist of $GABA_A$ and $GABA_C$ receptors, or (B, E) strychnine, an antagonist of glycine receptors. (C) Illustration of the difference filter computed by subtracting the temporal filters from after and before pharmacological application for each cell. (F, J, O, S) Average temporal filters from (F, J) excitatory and (O, S) inhibitory currents of $A_{OFF\text{-}S}$ (odd rows) and $A_{OFF\text{-}T}$ (even rows) ganglion cells in control (left) and cone-DTR (right) retinas under Ames (solid line) and (F, O) 100μM picrotoxin or (J, S) 5 μM strychnine (dashed line) as well as the difference between Ames and (F, O) picrotoxin (yellow) or (J, S) strychnine (green). (G, K, P, T) First and second principal components from (G, K) excitatory and (P, T) inhibitory temporal filter differences between (G, P) picrotoxin and Ames or (K, T) strychnine and Ames of each $A_{OFF\text{-}S}$ (warm colors) or $A_{OFF\text{-}T}$ (cool colors; refer to box plot colors in H for legend). Variance captured by each principal component noted on the corresponding axis. (H, L, Q, U) Box plots of first principal components (PC1) across cell types and conditions for the differences between (H, Q) Ames and picrotoxin or (L, U) Ames and strychnine from (H, L) excitation temporal filters and (Q, U) inhibition temporal filters. (I, M, R, V) Comparison of the difference

PC1 determined between (I, R) picrotoxin and Ames, and (M, V) strychnine and Ames for control and cone-DTR conditions for $A_{OFF\text{-}S}$ and $A_{OFF\text{-}T}$ ganglion cells from (I, M) excitatory or (R, V) inhibitory temporal filters. (N, W) Results of the comparison of PC1 and the interpretation of mechanisms for (N) excitatory temporal filters and (W) inhibitory temporal filters. P-values in box plots indicate rank sum comparison between each pair of conditions; p-values are corrected for multiple comparisons with the Bonferroni-Holm method (H, L, Q, U). P-values in scatter plots from a permutation test with correction for multiple comparisons (I, M, R, V). See also Table S2.

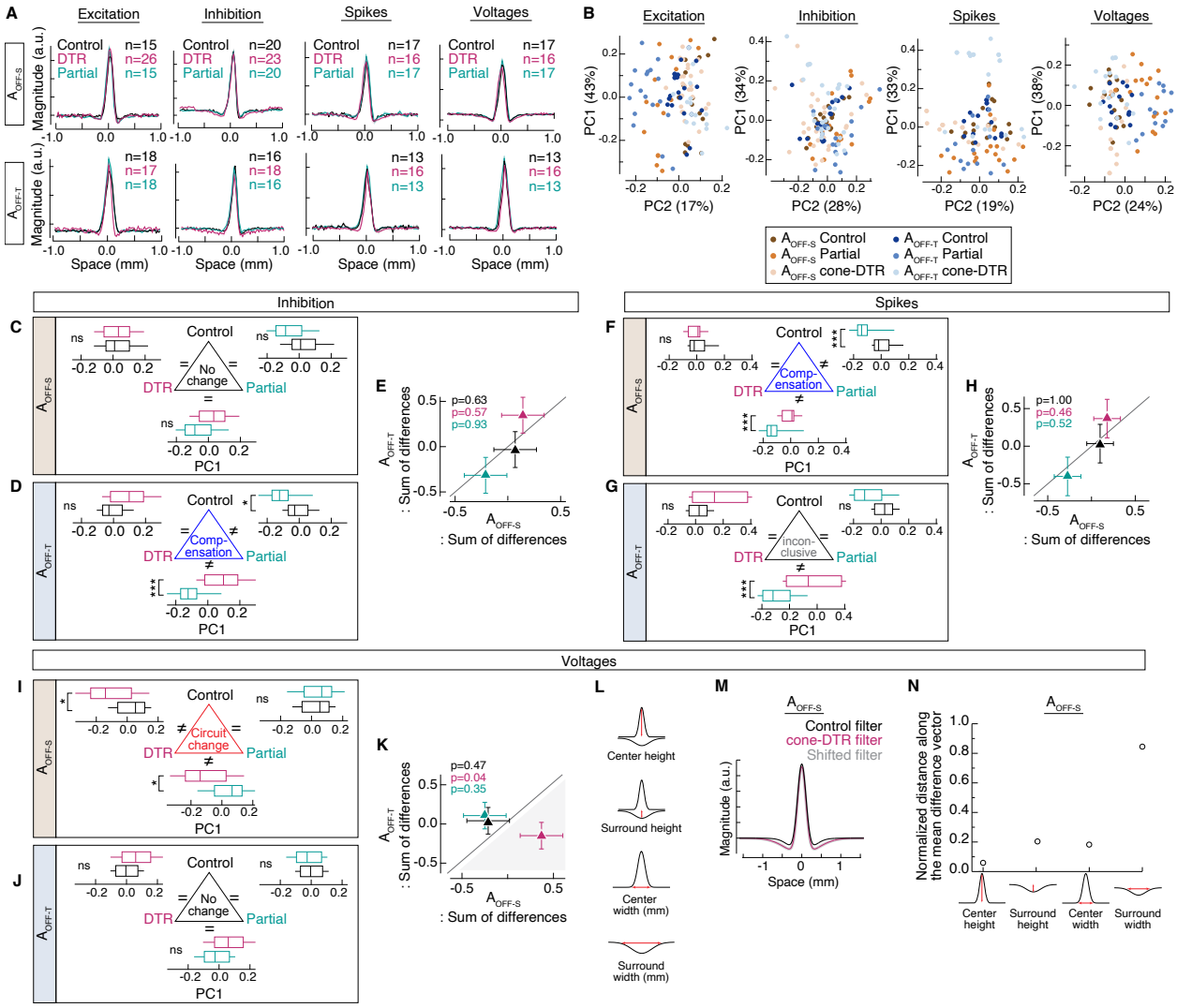

Figure 3. Partial cone loss causes differential changes in spatial filters of A_{OFF} ganglion cell types. (A) Average spatial filters from excitation, inhibition, spikes, and subthreshold voltages of (top) $A_{OFF\text{-}S}$ and (bottom) $A_{OFF\text{-}T}$ ganglion cells in control (black), cone-DTR (magenta) and partial stimulation (green). (B) Projections onto the first and second principal components for the spatial filters of each $A_{OFF\text{-}S}$ (warm colors) or $A_{OFF\text{-}T}$ (cool colors) for the three conditions from excitation, inhibition, spikes, and voltages. Variance captured by each principal component noted on the corresponding axis. (C-D, F-G, I-J) Box plots of first principal components (PC1) for (C, F, I) $A_{OFF\text{-}S}$ and (D, G, J) $A_{OFF\text{-}T}$ ganglion cells between conditions from (C-D) inhibition, (F-G) spikes, and (I-J) voltages, which showed significant differences across conditions. Interpretation of mechanisms in the triangle centers. (E, H, K) Comparison of sum of differences between $A_{OFF\text{-}S}$ and $A_{OFF\text{-}T}$ ganglion cells for PC1 from (E) inhibition, (H) spikes, and (K) voltages. Gray regions indicate where a significant difference was found. (L) Features extracted from spatial filters: center height, surround height, center width, and surround width. (M) Average spatial filters under control and cone-DTR conditions for $A_{OFF\text{-}S}$ ganglion cells, which show a significant difference, and a version of the control spatial filter shifted by multiple parameters to match the cone-DTR spatial filter. (N) Normalized distance between the spatial filter in control (ordinate = 0) and cone-DTR (ordinate = 1) when the control spatial filter is changed by each parameter. P-values in box plots indicate rank sum comparison between each pair of conditions; p-values are corrected for multiple comparisons with the Bonferroni-Holm

method (C-K). P-values in scatter plots indicate significant differences between $A_{OFF\text{-}S}$ and $A_{OFF\text{-}T}$ ganglion cells from a permutation test with correction for multiple comparisons (E, H, K). See also Figure S4, Table S3.

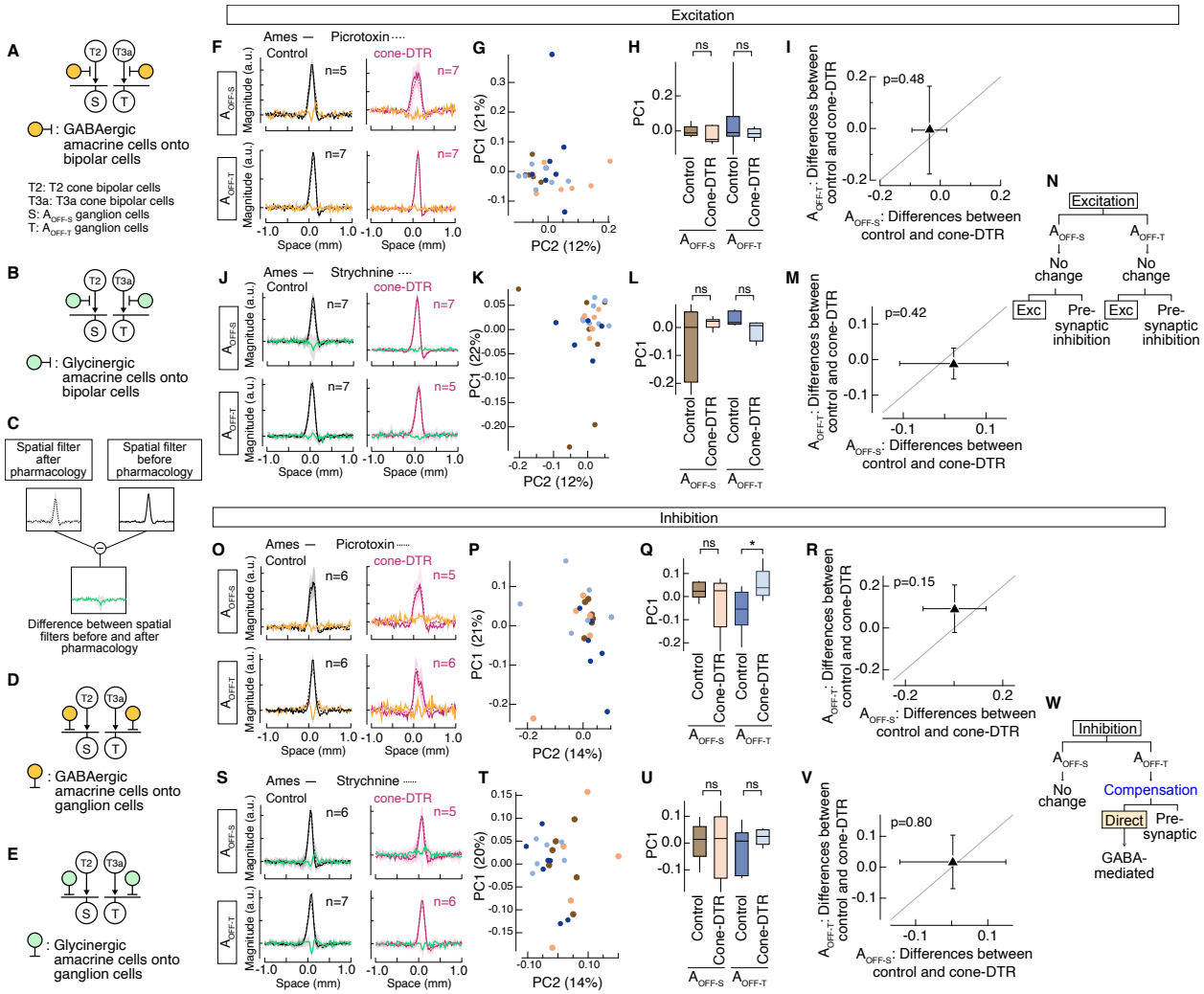

Figure 4. Partial cone loss causes excitation and direct GABAergic and glycinergic inhibition to mediate changes in the cone-DTR spatial filters of $A_{OFF\text{-}T}$ ganglion cells. (A-B, D-E) Schematic of retinal pathways leading to the (left) $A_{OFF\text{-}S}$ and (right) $A_{OFF\text{-}T}$ ganglion cells and the circuit motifs for direct excitation (white), presynaptic inhibition from (A) GABA (yellow) or (B) glycine (green), and direct inhibition from (D) GABA (yellow) or (E) glycine (green) that would be blocked by (A, D) picrotoxin, an antagonist of $GABA_A$ and $GABA_C$ receptors, or (B, E) strychnine, an antagonist of glycine receptors. (C) Illustration of the difference filter computed from subtracting the spatial filters from after and before pharmacological application for each cell. (F, J, O, S) Average spatial filters from (F, J) excitatory and (O, S) inhibitory currents of $A_{OFF\text{-}S}$ (odd rows) and $A_{OFF\text{-}T}$ (even rows) ganglion cells in control (left) and cone-DTR (right) retinas under Ames (solid line) and (F, O) 100μM picrotoxin or (J, S) 5 μM strychnine (dashed line) as well as the difference between Ames and (F, O) picrotoxin (yellow) or (J, S) strychnine (green). (G, K, P, T) First and second principal components from (G, K) excitatory and (P, T) inhibitory spatial filter differences between (G, P) picrotoxin and Ames or (K, T) strychnine and Ames of each $A_{OFF\text{-}S}$ (warm colors) or $A_{OFF\text{-}T}$ (cool colors; refer to box plot colors in H for legend). Variance captured by each principal component noted on the corresponding axis. (H, L, Q, U) Box plots of first principal components (PC1) across cell types and conditions for the differences between (H, Q) picrotoxin and Ames or (L, U) strychnine and Ames from (H, L) excitation spatial filters and (Q, U) inhibition spatial filters. (I, M, R, V) Comparison of the difference PC1 determined between (I, R) Ames and picrotoxin and (M, V) Ames and strychnine

for control and cone-DTR conditions for $A_{OFF\text{-}S}$ and $A_{OFF\text{-}T}$ ganglion cells from (I, M) excitatory or (R, V) inhibitory spatial filters. (N, W) Results of the comparison of PC1 and the interpretation of mechanisms for (N) excitatory spatial filters and (W) inhibitory spatial filters. P-values in box plots indicate rank sum comparison between each pair of conditions; p-values are corrected for multiple comparisons with the Bonferroni-Holm method (H, L, Q, U). P-values in scatter plots from a permutation test with correction for multiple comparisons (I, M, R, V). See also Table S4.

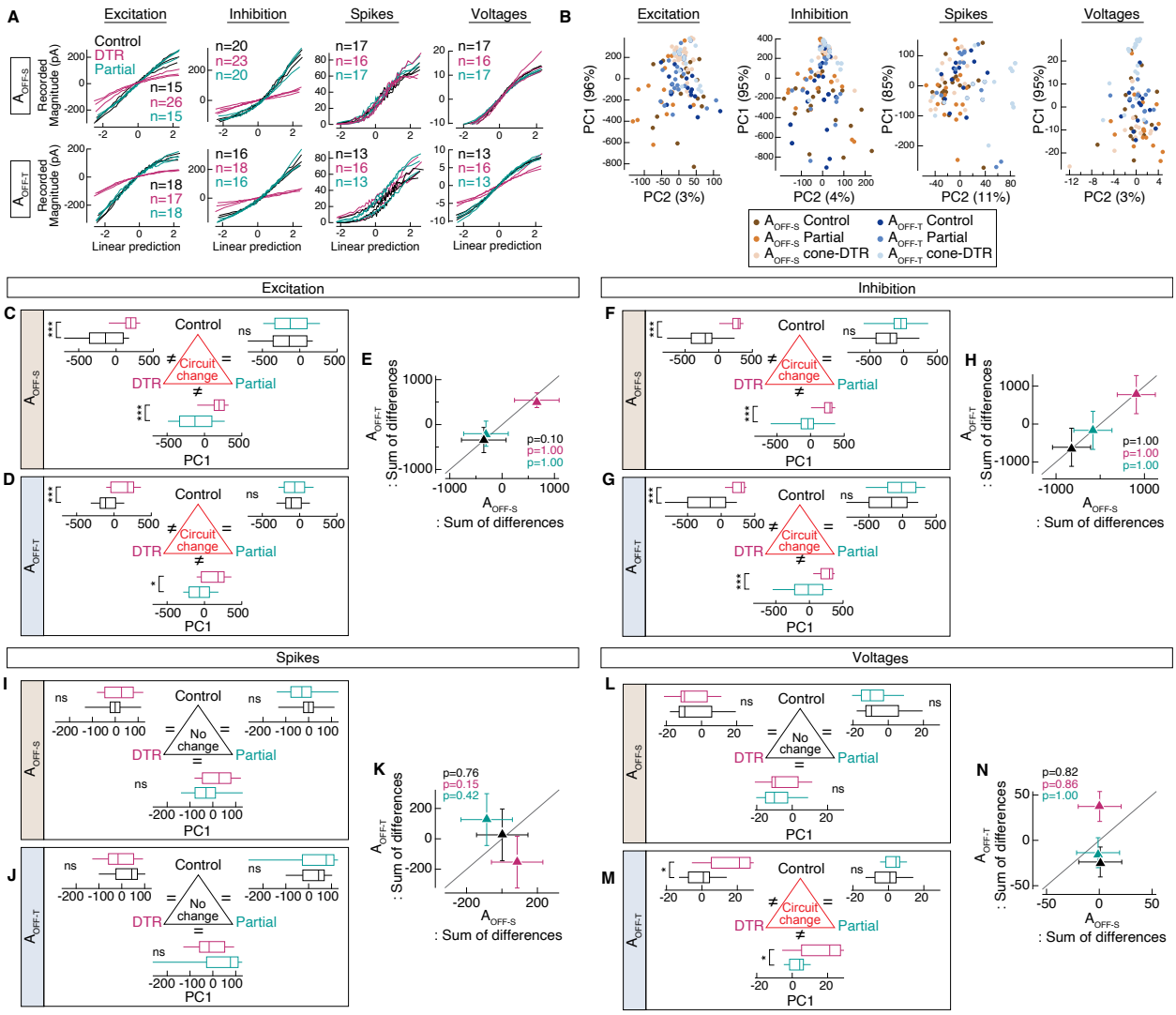

Figure 5. Partial cone loss causes responses of $A_{OFF\text{-}S}$ and $A_{OFF\text{-}T}$ ganglion cells to decrease. (A) Three exemplar nonlinearities from control (black), cone-DTR retina (magenta), and partial stimulation (green) for excitation, inhibition, spikes, and subthreshold voltages from individual (top) $A_{OFF\text{-}S}$ and (bottom) $A_{OFF\text{-}T}$ ganglion cells. (B) First and second principal components for the nonlinearity of each $A_{OFF\text{-}S}$ (warm colors) or $A_{OFF\text{-}T}$ (cool colors) for the three conditions from excitation, inhibition, spikes, and voltages. Variance captured by each principal component noted on the corresponding axis. (C-D, F-G, I-J, L-M) Box plot of first principal components (PC1) for (C, F, I, L) $A_{OFF\text{-}S}$ and (D, G, J, M) $A_{OFF\text{-}T}$ ganglion cells between conditions from (C-D) excitation, (F-G) inhibition, (I-J) spikes, (L-M) voltages. Interpretation of mechanisms in the triangle centers. (E, H, K, N) Comparison of sum of differences between $A_{OFF\text{-}S}$ and $A_{OFF\text{-}T}$ ganglion cells for the PC1 from (E) excitation, (H) inhibition, (K) spikes, (N) voltages. P-values in box plots indicate rank sum comparison between each pair of conditions; p-values are corrected for multiple comparisons with the Bonferroni-Holm method (C-D, F-G, I-J, L-M). P-values in scatter plots from a permutation test with correction for multiple comparisons (E, H, K, N). See also Table S5.

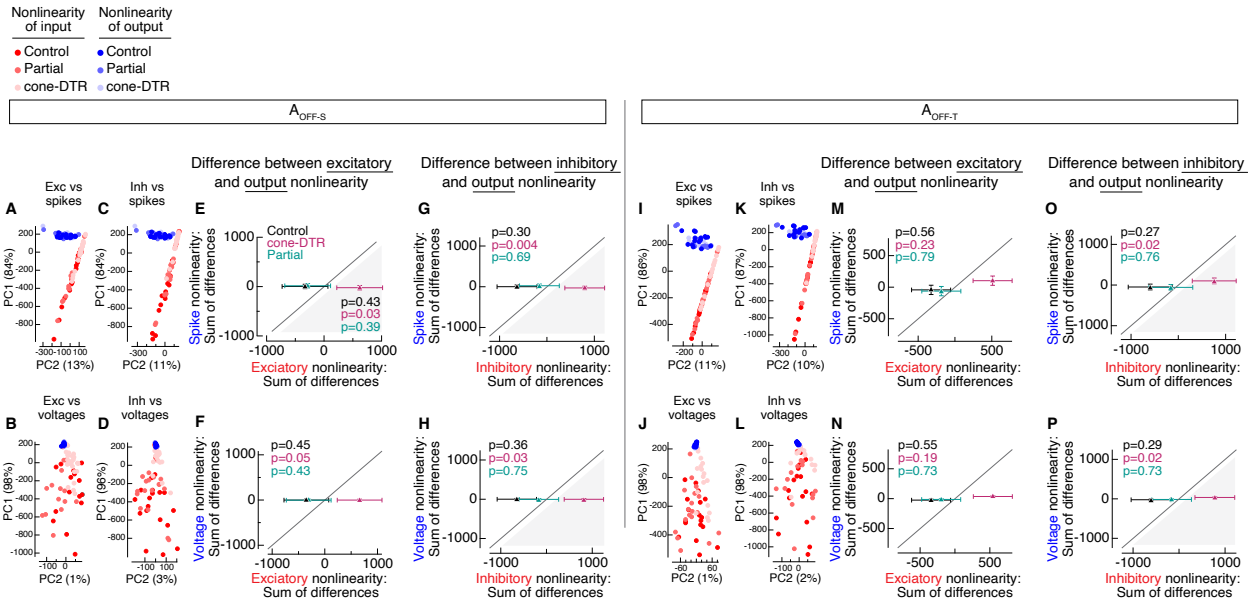

Figure 6. Partial cone loss has a differential impact on nonlinearities of input currents vs. output voltages and spikes. Principal component analysis was performed on the nonlinearities for excitation and spikes, excitation and subthreshold voltages, inhibition and spikes, inhibition and subthreshold voltages. Using the projection onto the first principal component of nonlinearities across conditions, we analyzed the sum of differences to determine differences between inputs vs. outputs. (A-D, I-L) First and second principal components for the nonlinearities of input currents (red) or output voltages or spikes (blue) for the three conditions of control, cone-DTR, and partial in (A-D) $A_{OFF\text{-}S}$ or (I-L) $A_{OFF\text{-}T}$ ganglion cells. Variance captured by each principal component noted on the corresponding axis. (E-H, M-P) Comparison of PC1 sum of differences between (E, M) excitatory current and spike nonlinearities and (F, N) excitatory current and voltage nonlinearities of (E-F) $A_{OFF\text{-}S}$ and (M-N) $A_{OFF\text{-}T}$ ganglion cells. (G-H, O-P) Comparison of PC1 sum of differences between (G, O) inhibitory currents and spike nonlinearities and (H, P) inhibitory currents and voltage nonlinearities of (G-H) $A_{OFF\text{-}S}$ and (O-P) $A_{OFF\text{-}T}$ ganglion cells. Gray regions indicate where a significant difference was found. P-values in scatter plots from a permutation test with correction for multiple comparisons between input and output nonlinearities. See also Table S5.

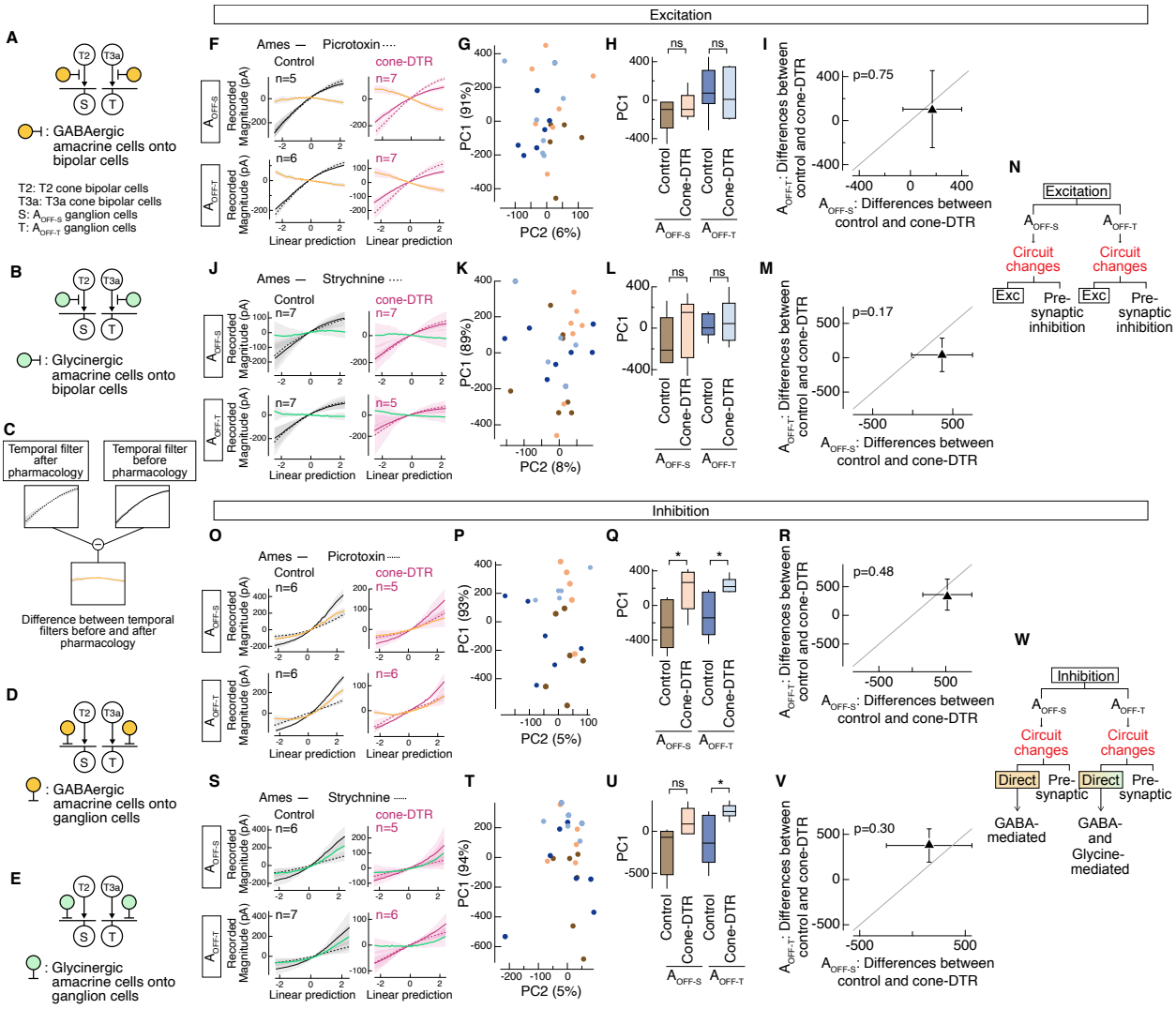

Figure 7. Partial cone loss causes excitation, direct GABA and glycine inhibition to mediate changes in the nonlinearity in cone-DTR nonlinearities of A_{OFF} ganglion cells. (A-B, D-E) Schematic of retinal pathways leading to the (left) A_{OFF-S} and (right) A_{OFF-T} ganglion cells and the circuit motifs for direct excitation (white), presynaptic inhibition from (A) GABA (yellow) or (B) glycine (green), and direct inhibition from (D) GABA (yellow) or (E) glycine (green) that would be blocked by (A, D) picrotoxin, an antagonist of $GABA_A$ and $GABA_C$ receptors, or (B, E) strychnine, an antagonist of glycine receptors. (C) Illustration of the difference nonlinearity computed from subtracting the nonlinearities from after and before pharmacological application for each cell. (F, J, O, S) Average nonlinearities from (F, J) excitatory and (O, S) inhibitory currents of A_{OFF-S} (odd rows) and A_{OFF-T} (even rows) ganglion cells in control (left) and cone-DTR (right) retinas under Ames (solid line) and (F, O) 100μM picrotoxin or (J, S) 5 μM strychnine (dashed line) as well as the difference between Ames and (F, O) picrotoxin (yellow) or (J, S) strychnine (green). (G, K, P, T) First and second principal components for the (G, K) excitatory and (P, T) inhibitory nonlinearity differences between (G, P) picrotoxin and Ames or (K, T) strychnine and Ames of each A_{OFF-S} (warm colors) or A_{OFF-T} (cool colors; refer to box plot colors in H for legend). Variance captured by each principal component noted on the corresponding axis. (H, L, Q, U) Box plots of first principal components (PC1) across cell types and conditions for the differences between (H, Q) picrotoxin and Ames or (L, U) strychnine and Ames from (H, L) excitation nonlinearities and (Q, U) inhibition nonlinearities. (I, M, R, V) Comparison of the

difference PC1 determined between (I, R) picrotoxin and Ames and (M, V) strychnine and Ames for control and cone-DTR conditions for $A_{OFF\text{-}S}$ and $A_{OFF\text{-}T}$ ganglion cells from (I, M) excitatory or (R, V) inhibitory nonlinearities. (N, W) Results of the comparison of PC1 and the interpretation of mechanisms for (N) excitatory and (W) inhibitory nonlinearities. P-values in box plots indicate rank sum comparison between each pair of conditions; p-values are corrected for multiple comparisons with the Bonferroni-Holm method (H, L, Q, U). P-values in scatter plots from a permutation test with correction for multiple comparisons (I, M, R, V). See also Table S6.

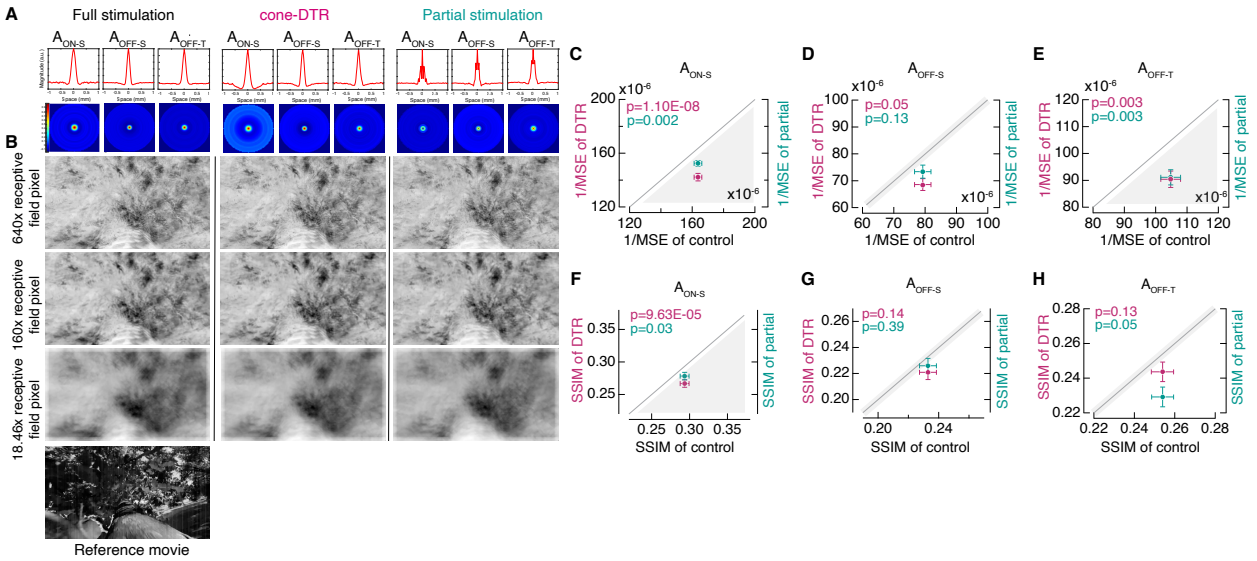

Figure 8. Natural movies filtered by the measured spatiotemporal receptive fields following partial cone loss are perceptually similar to those filtered by control retina. (A) Average linear spatial filters from bar noise stimuli (top) and 3D receptive fields (bottom) of $A_{ON\text{-}S}$, $A_{OFF\text{-}S}$, and $A_{OFF\text{-}T}$ ganglion cells under the following conditions: (1) full stimulation of control retina, (2) cone-DTR retina, and (3) partial stimulation of control retina. (B) Example frame of movies resulting from convolution of a reference movie (bottom) with each of three spatiotemporal filters at movie sizes 640, 160, 18.46 times the receptive field size. (C-E) Non-perceptual similarity index (1/MSE) averaged across movie-to-receptive field pixel ratios in conditions of control (abscissa), cone-DTR (left ordinate; magenta), and partial stimulation (right ordinate; green) for (C) $A_{ON\text{-}S}$, (D) $A_{OFF\text{-}S}$, and (E) $A_{OFF\text{-}T}$ ganglion cells. (F-H) Structural similarity index (SSIM) of convolved movies with the reference movies averaged across movie-to-receptive field pixel ratios in three conditions of control (abscissa), cone-DTR (left ordinate; magenta), and partial stimulation (right ordinate; green) for (F) $A_{ON\text{-}S}$, (G) $A_{OFF\text{-}S}$, and (H) $A_{OFF\text{-}T}$ ganglion cells. P-values from two-way ANOVA to compare differences between convolved movies under either cone-DTR or partial stimulation with the movies convolved by the control condition. Gray regions mark whether the p-value is not significant (along the line of slope unity) or significant (gray triangle). See also Figure S7, Table S8.